



**HAL**  
open science

# The influence of the cube component on the mechanical behaviour of copper polycrystalline samples in tension

B. Bacroix, S. Queyreau, D. Chaubet, E. Siv, Th Chauveau

## ► To cite this version:

B. Bacroix, S. Queyreau, D. Chaubet, E. Siv, Th Chauveau. The influence of the cube component on the mechanical behaviour of copper polycrystalline samples in tension. *Acta Materialia*, 2018, 160, pp.121-136. 10.1016/j.actamat.2018.08.044 . hal-02340566

**HAL Id: hal-02340566**

**<https://hal.science/hal-02340566>**

Submitted on 30 Oct 2019

**HAL** is a multi-disciplinary open access archive for the deposit and dissemination of scientific research documents, whether they are published or not. The documents may come from teaching and research institutions in France or abroad, or from public or private research centers.

L'archive ouverte pluridisciplinaire **HAL**, est destinée au dépôt et à la diffusion de documents scientifiques de niveau recherche, publiés ou non, émanant des établissements d'enseignement et de recherche français ou étrangers, des laboratoires publics ou privés.

# **The influence of the Cube component on the mechanical behaviour of copper polycrystalline samples in tension**

B. Bacroix\*, S. Queyreau, D. Chaubet, E. Siv and Th. Chauveau

LSPM – CNRS, Université Paris 13, 99 av. J.B. Clément, 932430 Villetaneuse, France

\* Corresponding author, [brigitte.bacroix@univ-paris13.fr](mailto:brigitte.bacroix@univ-paris13.fr)

## Abstract

Copper tensile samples were prepared by various thermomechanical treatments (rolling and annealing) producing different initial textures, characterized mainly by an increasing Cube component. These samples were characterized microstructurally (orientation, grain boundary and grain size distributions) and mechanically (tensile stress – strain curves, hardness, dislocation density). It is found that an increase of the Cube percentage leads to an increase of the initial yield stress and to a decrease of the hardening rate at high strains. The macroscopic mechanical behaviour is compared with simulations performed with a simple Taylor type model including anisotropic plastic behaviour and dislocation-based constitutive equations. We show that the proposed modeling allows to reproduce all experimental curves with a limited number of adjusted parameters and that dynamic softening is more active in the Cube orientation than in any other present orientation. This is also confirmed by the EBSD and X-Ray data. As a result, the Cube orientation is shown to be softer in terms of texture and hardening rate. The opposite strengthening effect observed on the initial yield stress is shown to be due to heterogeneous grain size distributions resulting from complex recrystallization mechanisms.

Keywords: crystalline plasticity, dislocation density, XRD, cube orientation, dynamic recovery

## 1. Introduction

It is important to be able to describe correctly the mechanical behavior of polycrystalline FCC metals and alloys, especially in the context of metal forming simulations involving strongly anisotropic materials. In this context, commercially pure copper, while not being the most industrially used metal, has long been an ideal candidate to experimentally investigate and theoretically validate the basic mechanisms of hardening, softening [1-3] or recrystallization in metals [4, 5]. The attractiveness of copper is certainly justified since it combines (i) a relatively strong and discrete texture after rolling and annealing [6], that facilitates the investigation of the influence of individual texture components on the mechanical behavior, (ii) a capacity of developing some specific grain boundary (GB) distributions, because of the facility to obtain e.g. annealing twins in copper alloys, (iii) an already well-documented description of the basic mechanisms of plasticity and recrystallization involved during thermomechanical processing [7-10], and of dislocation patterning [11-13] and / or grain refinement through severe plastic deformation processes [14-16]. As a result, a lot of phenomenological or physically-based models have already been developed and tested on copper alloys, for example in the case of the prediction of textures [17] or more simply for the description of the macroscopic mechanical behavior (like e.g. [3, 13, 18]), capable of taking into account the influence of the crystallographic and morphological textures, of the grain size, grain boundary and dislocation density distributions on the macroscopic response [19-25]. But, in spite of the tremendous documentation already available on the subject, the issue of a predictive model, capable of reproducing the mechanical behavior of various copper alloys, associated with various textures and grain size distributions is still not closed. In particular, the influence of the cube component on mechanical behavior – which can develop

quite dramatically during recrystallization – is still not completely well understood. This is true for copper alloys but also for other FCC metals, like e.g. the aluminum or nickel alloys.

When considering past investigations on single crystals or polycrystals containing a significant proportion of cube-oriented grains, some contradictory data can be found in the literature. In the case of Cu single crystals deformed in tension, it is often reported that the particular symmetry of the cube orientation involves the simultaneous activation of up to 8 slip systems which are equally stressed, which in turn produces a strong hardening rate in the early deformation steps. In order to compensate this strong hardening rate, recovery is then activated at relatively low strains, leading to a macroscopic parabolic work-hardening type as in [100] single crystals. This contrast to a more linear hardening observed in other orientations, such as [111] [26, 27]. In other studies concerning aluminum however, the [100] orientation is reported to be softer than [111] from the very beginning of the deformation, while presenting also an enhanced recovery stage at moderate strains [28]. In polycrystalline samples, the particular symmetry of the cube orientation is also mentioned to justify an enhanced recovery during and after deformation in copper, but mainly in rolling [1, 8], because of the activation of two pairs of orthogonal systems, which are claimed to be unable to form stable junctions and thus may undergo thermally activated recovery much easier than other orientations [8]. Recently, Hutchinson showed as well that this particular softening mechanism responsible for enhanced recovery in cube grains in rolling was not so efficient in tension, in spite of the activation of orthogonal systems for this loading path [29]. Enhanced recovery has however been observed in transmission electron microscopy (TEM) in cube-oriented grains in copper samples deformed in tension [12], in consistence with other data obtained by X-ray Diffraction [23].

It seems obvious then that the hardening behavior of one particular orientation – like e.g. the Cube orientation – depends in a complex way of the boundary conditions imposed to the

grain presenting the selected orientation (single crystal versus single grain within a polycrystalline sample, tension versus plane strain compression), of the stacking fault energy of the material (copper versus aluminum), but also on the amount of strain (in particular for the initiation of hardening / softening stages), on the texture (including the direct neighbouring grains) and microstructure (grain size distribution) of the material. The aim of the present paper is thus twofold: (i) to bring some additional data allowing to go further into the understanding of the influence of cube-oriented grains on the overall mechanical behavior of polycrystalline samples, and (ii) to test the validity of the recently proposed hardening / softening law [19] in tension. The present paper is thus organized as follows: the material, imposed thermomechanical treatment and experimental techniques are described in **Section 2**, the texture and microstructural features of the studied materials are reported in **Section 3**, whereas the mechanical data obtained in tension, as well as the dislocation density estimations performed from X-ray diffraction and Electron Back Scattering Diffraction (EBSD) are detailed in **Section 4**. In **Section 5**, the experimental curves are reproduced by a polycrystalline model including the recently proposed physically-based hardening / softening law [19], and the comparison between experimental and calculated data allows to draw some conclusions on the role of the cube component on the overall behavior of the selected materials. Some general conclusions are finally drawn in **Section 6**.

## **2. Material, thermomechanical processing and experimental methods**

### ***2.1. Material and thermomechanical processing***

The selected material is some OFE Copper (Oxygen Free Electronic Grade), furnished by the French company GRISET, in the hot-rolled state and in the shape of a thick plate of initial

thickness equal to 12.5 mm. This material contains at least 99.99% copper, corresponding to a residual impurity content of less than 100 ppm (and mainly Ag, S, Fe, Ni). The texture of the as-received material is a typical rolling texture, mainly composed of the so-called Bs, S and Cu orientations [1]. This material is then cold-rolled in our laboratory rolling mill in several passes (the maximal reduction per pass ranges from 1 mm in the early passes to 0.5 mm in the final ones), to achieve different final thicknesses of 3.75mm, 2.02, 0.87 and 0.54 mm, which correspond to 73, 84, 93 and 96% rolling reduction respectively. It was then checked that the textures of the cold-rolled samples remained consistent with those previously determined [1]. Based on our previous investigation on recrystallization processes in copper [1], some small pieces were cut and annealed at temperatures below 400°C during varying times between 15 min and 2 hours under vacuum, in order to determine the conditions for full recrystallization.

Annealing was followed by mechanical grinding with silicon carbide paper of grade 220 up to grade 4000, and polishing with a diamond solution up to 1  $\mu\text{m}$ , in order to perform hardness measurements (with a Buehler instrument using a diamond Vickers (HV0.05) indenter). The samples were then electropolished for X-Ray measurements of the texture or additionally polished with Oxide Polishing Suspension (OPS) in order to characterize the microstructure in a scanning electron microscope (SEM).

## ***2.2. Characterization of the fully recrystallized states***

The global crystallographic texture of each annealed sample was characterized using X-Ray Diffraction (XRD). For that purpose, an INEL (four-circle) goniometer with Co  $k\alpha$  radiation source ( $\lambda = 0.17902\text{nm}$ ) was used. The {111}, {200} and {220} pole figures were measured with a maximum tilt angle of 80° and the Orientation Distribution Functions (ODF) were calculated with the Labotex® software, which is based on the ADC (Arbitrary Defined Cell)

iterative discrete method, which allows to describe the texture as a discrete set of orientations and associated volume fractions [30]. The number of orientations can be varied, according to the texture intensity and desired precision. In the present case, in order to extract from these data the percentages of some specific texture components, the initial number of orientations describing the ODFs has been taken equal to 20,000.

Electron Back Scattering Diffraction (EBSD) was performed on a Cambridge S360 SEM equipped with the Orientation Imaging Microscopy (OIM<sup>®</sup>) software from Tex-SEM laboratories. Scans from  $100\ \mu\text{m} \times 100\ \mu\text{m}$  to  $400\ \mu\text{m} \times 400\ \mu\text{m}$  were performed with a step of  $0.3\ \mu\text{m}$  for the smaller scans or  $0.6\ \mu\text{m}$  for the largest scans. The data processing of the raw data was then performed using the TSL OIM<sup>®</sup> Analysis 7 software, especially to get information regarding the density and nature of the boundaries in the microstructure as well as the grain size distribution. Grain boundaries were classically defined by the minimum misorientation angle of  $15^\circ$  (and are called Large Angle Grain Boundaries, LAGB). During processing, grains that had a size of less than 2 pixels were removed using the provided grain dilation method (with a tolerance on misorientation angle of  $5^\circ$ ). Twin boundaries were defined as interfaces with a misorientation of  $60^\circ \pm 5.8^\circ$  around a  $\langle 111 \rangle$  crystal axis).

Fig. 1 shows the microhardness values measured for the imposed annealing conditions associated with the smallest annealing time. Based on these data, the selected conditions for complete recrystallization associated with each rolling reduction are presented in Table 1. The samples, for which microstructural features and mechanical data are reported below, have thus been deformed between 73 and 96% cold rolling (CR) strain and then annealed 15 min at temperatures varying between  $350^\circ\text{C}$  (for 73 % CR) and  $200^\circ\text{C}$  (for 96% CR). Based on these hardness measurements, they are assumed to be completely recrystallized.

### ***2.3. Tensile tests and characterization of the hardening state***

Some small tensile samples were then cut out in the 4 rolled and fully recrystallized sheets, before being deformed with the tensile mini-machine developed at LSPM [31]. The dimensions of the central part of the specimens were selected to be 5 mm for the initial length, and 2.5 mm for the initial width; the initial thickness was that of the rolled sheet (that is 3.76, 2.02, 0.87 or 0.54 mm, depending on the rolling strain). The load and crosshead displacement were then registered during the tensile tests performed at a displacement rate of  $10^{-3} \text{ s}^{-1}$ . As a result of the varying thickness of the samples, the influence of the stiffness of the machine on the resulting load – displacement curve strongly varies from one sample to the other. Thus, in order to perform the identification of the plastic parts only, the plastic strain – stress curves are then deduced from the measurements by taking out the apparent elastic part (which includes the elastic deformation of the machine and of the sample), and by validating the so-obtained final plastic strain (close to 25%) by the measurements of the final dimensions of the specimens. The yield stress is evaluated from these corrected curves at 0.2% plastic strain.

The surface of the samples was again polished in order to perform some EBSD and dislocation density measurements after tension. For the second ones, some X-ray line profiles associated with the principal texture components found after tension (following cold-rolling and full recrystallization annealing) were determined with the LSPM high resolution four circle diffractometer equipped with a rotating anode - BRUKER™ SRA 18 (CoK $\alpha$ 1 radiation,  $\lambda = 0.1788976 \text{ nm}$ ). The long fine X-ray source was combined with an INEL™ two bounce channel cut monochromator (Ge {220}). The diffracted intensity was recorded with an INEL™ linear position-sensitive detector ( $\Delta 2\theta = 8.388 \text{ E-}4^\circ$ ) placed at the distance of 1 m from the center of rotation of the four circle diffractometer. This set up is characterized by negligible spectral dispersion. The method used to extract the dislocation density from the peak profiles is detailed in Section 4.

### 3. Texture and microstructure evolutions during annealing and tension

The pole figures determined after full recrystallization annealing and recalculated from the ODFs are presented in Fig. 2 for the 4 different states. The first two states (73 % CR – annealed at 350°C or 84% CR – annealed at 300°C) are associated with moderate textures presenting a lot of scattering (at least when considering the pole figures). When the rolling strain is increased, the textures become more and more intense and the Cube component appears clearly on these figures. The maximal intensity in the {200} pole figure increases from about 4 (x random intensity) for the (73 % CR – annealed at 350°C) sample to 34 for the (96 % CR – annealed at 200°C) sample. In order to be more quantitative, the volume fractions of 50 orientations a priori selected have been calculated from the ODFs. These selected 50 orientations are (i) the 10 orientations (grouped into 5 families) which classically compose the rolling and annealing textures in FCC materials that is the orientations called: Cube = {100}<001> (1 single orientation), Goss = {110}<001> (1 orientation), Cu = {112}<111> (2 orientations to respect the orthotropic symmetry of the rolling process), Bs = {110}<112> (2 orientations) and S = {123}<634> (4 orientations), together with (ii) their 40 twinned orientations (4 twinned orientations for each rolling or annealing texture component, corresponding to a rotation of 60° around one of the four <111> axes, again grouped in 5 families, CubeT (4 orientations), GossT (4 orientations), CuT (8 orientations), BsT (8 orientations) and ST (16 orientations), which finally makes a total of 10 orientation families plus the rest composed of all remaining orientations. The volume fractions of all these orientation families have been calculated from the ODFs based on 20000 discrete orientations, and by considering a tolerance of 15° around each texture component (the same tolerance value has been used for the calculations of the volume fractions from the EBSD

maps also presented below, see Table 2). It is worth pointing out that in the list of 50 orientations (in which the non-twinned orientations are listed first), some are quite close, and can thus overlap because of the considered tolerance. In that case, the volume fraction of the 1<sup>st</sup> orientation considered in the list is increased at the expense of the second, which has the consequence of overestimating the proportions of the non-twinned orientations to the expense of the twinned ones. One exception has been made though for the CubeT orientation – which is only separated by a misorientation of 12.3° from the S orientation – which has been considered before the S component: in this case, we can say that the proportion of the CubeT orientation is overestimated compared to that of the S orientation, but we will see later that it better corresponds to the EBSD maps after recrystallization. The result of such a calculation is presented in Fig. 3 for the tested materials. The contribution of Cube and CubeT orientations to the ODFs clearly increases with increasing prior rolling reduction rate, while the intensity of other components, including the rest, is decreasing. The two components Cube and CubeT become the main ones in the sample which has been cold rolled up to 96% and fully annealed at 200°C.

Some typical EBSD orientations maps obtained on the fully recrystallized materials are now shown in Fig. 4. These maps are consistent with the X-ray pole figures, and present a significant spread in the distribution of the orientations after 73% rolling followed by annealing at 350°C, and a major Cube component (with twinning contribution) after 96% rolling followed by annealing at 200°C. It is also clear that annealing twins are present in a lot of grains of various orientations. The corresponding grain size distributions are presented in Fig. 5: the grain size is represented here by an equivalent diameter (in  $\mu\text{m}$ ), and the area fraction associated with each grain size is evaluated. It is worth pointing out that the average grain size has been calculated here by considering all grains delimited by LAGB (including the twin boundaries), which means that, unlike in some other studies [32], the twinned

components, which influence the mechanical properties, are also considered as individual grains in this calculation. The spread of grain size is also found to be quite large, especially for the (73 % CR – annealed at 350°C) sample. As a result, the average grain size first increases and then decreases with the increase of the amount of prior strain. The EBSD maps of Fig. 4 are representative of recrystallized samples, resulting from two simultaneous mechanisms which are nucleation and growth of new grains of orientations generally included within the dispersion of orientations of the deformed grains, and twinning, which can occur either by nucleation or by a growth accident [32, 33]. This competition generally leads to quite heterogeneous microstructures, as often reported for copper (see e.g. [34]). If we can conclude from these maps that the number of nuclei (and thus the final grain size) obviously depends on the amount of prior strain (and thus of the stored energy within the grains), it is interesting to note that annealing twins are present both in small and large grains, and that the size of the twinned parts also depends on the size of the grains within which they form. The Twin Boundaries (TB) also appear as mostly straight, which is often said to be an indication of their formation by nucleation rather than by growth [32, 35]. The relation between grain size and twin boundary proportion is illustrated in Fig. 6. As in the case of nickel alloys, the amount of TB clearly increases with the average grain size [32]. We also notice that the principal orientations of the twinned boundaries change with the texture: consequently, in the (96 % CR – annealed at 200°C) sample, a lot of twins are included in the cube-oriented grains (thus validating the choice explained above for the determination of the volume fractions of principal texture components), which induces a main orientation of the twin boundaries at 45° from the rolling direction. This orientation may also have an influence on the mechanical properties as demonstrated in Zhang et al. [36], that showed that it was indeed the softest orientation for TB. Table 2 lists the key quantitative features of the microstructure that can be extracted from EBSD maps. Due to the observed dispersion in grain size and morphology,

both simple and area-weighted average GS are indicated in Table 2, as well as the calculated standard deviation. As this parameter is quite high for all examined samples, a simple average estimation of the grain size would not be relevant. As suggested in [37, 38], we also calculated a so-called representative grain size  $D_R$ , which takes into account the dispersion around the average value, according to the following formula

$$D_R = \exp\left(M + \frac{11}{4}S^2\right) \quad (1)$$

where  $M$  and  $S$  are the mean and standard deviation of the grain size distribution function, respectively. The grain size distribution function is assumed to be lognormal [38].

Fig. 7 presents some EBSD orientations maps measured after 23% plastic strain for the two extreme cases, namely for the (73 % CR – annealed at 350°C) and (96 % CR – annealed at 200°C) cases. A limited texture evolution is visible through the slight change in color distribution (compared with Fig. 4). The recalculation of the ODFs from the pole figures measured by XRD after tension also confirms an increase of the Cube component and a decrease of the CubeT component during tension. This was indeed expected, since the Cube component is known to be stable during tension, whereas the CubeT component is known to be unstable (in this orientation, the tensile axis is located at 17° from a <112> direction). The pole figures obtained from XRD measurements after tension (Fig. 8) allow illustrating this evolution, and the percentages of the two main texture components, clearly identified as Cube and CubeT, evaluated from the ODFs are presented in Table 3.

This microstructural investigation shows clearly that the amount of Cube increases with the amount of strain prior to recrystallization annealing; additionally, the spread of the GS distribution, which is quite high for all samples, tends to slightly decrease with the amount of Cube component.

#### **4. Mechanical data and dislocation densities measurements**

Fig. 9 now presents the true stress – true strain curves obtained in tension up to about 25% after the 4 investigated thermomechanical treatments. In spite of a strong variation in the apparent elastic part of the curves due to the variation in the thickness of the samples, the comparison of the stress levels and hardening shapes of the present curves to some curves from the literature allows to conclude that they are consistent with the ones already published for copper samples [25, 29, 39], even though the texture and amount of twins is not always documented for the already published curves. We can also notice that the hardening rate is quite linear for the two (73% CR – annealed at 350°C) and (84% CR – annealed at 300°C) samples whereas it becomes more parabolic as the Cube component increases within the texture (see also the hardening curves presented below in Fig. 14). It is also clear that the level of stress – and especially of the yield stress – increases with the amount of Cube component, which is in contradiction with the sole effect of texture on yield stress. The Taylor factor – which represents the sole effect of texture on the mechanical response – has been calculated for tension from the textures measured before and after tension (see section 5 for the details of the calculation): the data presented in Table 4, demonstrate that, although this factor does not evolve much with the texture or with the tensile strain, it slightly decreases with an increase of the Cube orientation percentage. Thus, the texture cannot explain the observed yield stress evolution. The influence of the grain size on the yield stress is now presented in Fig. 10, for which both classical (simple or area-weighted average) and representative average grain sizes have been considered. A linear fit has been performed for the 3 different representations and the correlation factor R found for each fit is mentioned in the figure. The presented data are clearly more consistent with the modified Hall-Petch law proposed by Raesinia and Sinclair [38] to account for the dispersion in the grain size distribution, than with the usual ones, as proposed e.g. by the OIM software. The observed

evolution of the grain size distributions may thus explain the increase of the initial yield stress with the increase of the Cube and CubeT components associated with a decrease of the GS distribution spread.

For the evaluation of the dislocation density, XRD has been used first. From the pole figures measured after tension, we were able to identify the diffracting positions allowing, as much as possible, the separate analysis of the two main orientations Cube and CubeT (since the percentage of these two main components are quite low for one of the investigated samples (that cold rolled up to 73% and then annealed at 350°C), the consideration of any other orientation is useless). These positions are shown in Fig. 11 for the two main peaks. We see that in fact the two orientations are well separated only on the {200} pole figure. For these two orientations, diffracted intensity was thus measured along the diffracting vector at Bragg angle values in  $\theta$  and  $2\theta$  on {111}, {200}, {220}, {222} and {311} diffracting planes according to the positions listed in Table 5. Some examples of Bragg peaks, normalized and centered, are shown in Fig. 12. The normalization is necessary due to the fact that the counting parameters are not always the same, since they depend on the actual spread of the scanned peak as well as on the intensity of the diffracting orientation. It is worth mentioning that the signal to noise ratio varies between  $10^2$  in the worst case to  $10^3$  in most of the cases, which is acceptable, although this ratio is somewhat higher than when obtained from synchrotron measurements [40]. It is also interesting to note that the peaks associated with the (96 % CR – annealed at 200°C) sample present some asymmetry. In order to confirm that this asymmetry is solely due to the material response, the same Erreur ! Signet non défini. peak, measured in the same conditions on an undeformed copper single crystal is also plotted in Fig. 12. It is clear that this peak is quite fine and symmetrical. As a result, we can conclude that the asymmetry observed on the peaks measured on deformed samples is a signature of a

possible asymmetry of the dislocation microstructure of the samples. This point is further commented below.

In order to extract from these measurements the dislocation density, we first assume that both broadening and shape of the diffraction peaks may be affected only by the presence of dislocations. It is a reasonable assumption, since, due to the initial large grain size and moderate strain, the size effect can be neglected in the present case. Then, a Fast Fourier Transform (FFT) analysis of the profiles based on the ‘‘modified Warren – Averbach model (MWAM)’’ [41] is carried out. This technique was found to be very efficient for the analysis of textured materials, even in the presence of a slight asymmetry [42]. The Fourier coefficients can be extracted for the analysis of the profile broadening. To do so, the Bragg peak  $I(2\theta)$  is first expressed in the crystal reciprocal lattice space  $I(\mathbf{K})$ , with  $\mathbf{K}$  being the diffraction vector. According to the MWAM model, the coefficients of the Fourier Transform  $A(L)$  of  $I(\mathbf{K})$  reads for small values of  $L$ ,

$$\ln|A(L)| = -\frac{\pi b^2}{2} \rho_{XRD} L^2 \ln\left(\frac{R_e}{L}\right) K^2 \bar{C} + Q \left(\frac{\pi b^2}{2}\right)^2 L^4 \ln\left(\frac{R_2}{L}\right) \ln\left(\frac{R_3}{L}\right) (K^4 \bar{C}^2) + o(L^6) \quad (2)$$

Here,  $L$  corresponds to a physical length in the crystal in the direction of the diffraction vector,  $K$  is the norm of the diffraction vector  $\mathbf{K}$  ( $K = 2 \sin \theta / \lambda$ , with  $\lambda$  the wavelength),  $b$  the norm of the Burgers vector of the dislocations,  $\rho_{XRD}$  is the dislocation density we are looking for, and  $R_e$  an outer cut-off radius for the dislocations ( $R_e \approx 1/\sqrt{\rho_{XRD}}$ ). In the last term of Eq. 2,  $Q, R_2, R_3$  are additional material parameters. The dimensionless coefficient  $\bar{C}$  is the average contrast factor of the dislocations present within the material – also used in TEM – which accounts for the anisotropy of the elastic strain field created by the dislocations [42]. This factor can be calculated as long as some hypotheses are made about the number of slip systems populated by dislocations and the possible dislocation types present in the material. In the present case, we consider for simplification that all possible slip systems are taken into

account and assumed to be equally populated, and that we have a 50% - 50% mixture of screw and edge dislocations. The dislocation density  $\rho_{XRD}$  has then been extracted from all measured profiles (not all shown in Fig. 12) by a classical minimization procedure [43], for each of the two considered components (see Table 6). It is worth recalling that this so-obtained dislocation density does include both the so-called geometrically necessary dislocations (GND), which generally constitute “hard” subgrain boundaries as well as the so-called statistically stored dislocations (SSD) which are dispersed within the dislocation cells which are thus considered to be “softer” zones. It has been recently shown that, when the densities of these two populations are roughly equal, the resulting X-ray profiles are symmetrical [40], the asymmetry produced by the harder zones being compensated by the one produced by the softer zones. The observed asymmetry mentioned above could thus be due to different populations of these two types of dislocations in the present case. This point will again be discussed later.

A second estimation of dislocation density can be made from the EBSD maps, but it then concerns solely the geometrically necessary dislocations (GND), i.e. the ones associated with misorientations at grain or subgrain boundaries [13]. The local density of GND is classically described by the following expression

$$\rho_{GND} = k \frac{\beta}{xb} \quad (3)$$

in which  $\beta$  is the misorientation at the considered point,  $x$  the distance between two measurements and  $k$  a constant that depends on the type of dislocations. It has been shown in a recent study [44] that using Nye’s tensor [45] for the descriptions of lattice distortions and rotations leads to Eq. (3) with  $k = 3$ . All recent studies using this equation thus make use of this value for the constant  $k$  [46]. The misorientation is then most often represented by the KAM (Kernel Average Misorientation) parameter by considering 1 to 3 EBSD measurement steps for  $x$  (we have considered 3 steps in the present case, in order to obtain a satisfactory

precision [47]). This parameter is an estimate of the local misorientation, calculated as the average of the misorientations between one given point and its nearest neighbors, excluding those which are not located within the same grain. The values calculated for individual components along with values for the whole maps are added to Table 6, together with the value  $\rho_M$  extracted from the tensile curves according to the Taylor formula

$$\sigma = M\alpha\mu b\sqrt{\rho_M} \quad (4)$$

with  $\alpha = 0.35$  as often mentioned in the literature for FCC metals [48],  $M$  the Taylor factor (see Table 4),  $\mu$  the mean shear modulus and  $b$  is the magnitude of the Burgers vector (here  $\frac{1}{2}\langle 111 \rangle a_0$ ). Although these data are scattered, it is interesting to note both XRD and EBSD lead to a dislocation density generally lower in the Cube orientation than in the CubeT orientation or in the whole polycrystal after 25% tensile strain. It is especially clear for the material tested after 96% rolling and annealing, for which, due to the relative high percentages of the two considered orientations, the XRD values seem to be statistically much more significant than after 73% rolling and annealing. Also, it is clear that  $\rho_{GND}$  is systematically lower than  $\rho_{XRD}$ , since both GND and SSD types of dislocations are taken into account by XRD [40]. It is rather striking that the estimates of these two densities  $\rho_{XRD}$  and  $\rho_{GND}$ , while obtained with different procedures based on simplifying assumptions, are consistent with some values of  $\rho_{GND}$  and  $\rho_{SSD}$  obtained in copper deformed in tension up to a slightly larger strain (40%) through TEM measurements [12] if we consider that we have in the present case,  $\rho_{SSD} = \rho_{XRD} - \rho_{GND}$ . From this equation, we get  $\rho_{SSD} \cong \frac{1}{2}\rho_{GND}$  for the (73% CR – annealed at 350°C) sample (as in the quoted TEM study), and  $\rho_{SSD} \cong \frac{1}{10}\rho_{GND}$  for the (96% CR – annealed at 200°C) sample. This rather low factor between  $\rho_{SSD}$  and  $\rho_{GND}$  may explain the observed asymmetry of the peaks.

In any case, the present XRD and EBSD measurements which establish that both GND and total dislocation densities are lower in the Cube orientation than in the other orientations composing the texture after 25% strain are also in agreement with some other data recently obtained on an isotropic copper sample [49]. This material, which presents a smaller average grain size than the present one, has also been annealed up to complete primary recrystallization and deformed in tension up to 20%. A close look at a local EBSD map obtained after tension and presenting the KAM value for few grains including annealing twins, confirms that the KAM (and thus  $\rho_{GND}$ ) is higher in twinned regions than in Cube oriented grains (see Fig. 13). Also, some strong KAM variations, indicating the presence of subgrain boundaries, associated with the fragmentation of the grain resulting from local reorientation, are also visible within the CubeT oriented grains, and not within the Cube oriented ones (which are indeed stable in tension).

To summarize these mechanical data, we can say that a high cube percentage induces two contradictory effects on the mechanical response in tension of the investigated samples, which are an increase of the yield stress due to complex recrystallization mechanisms resulting in the reduction of the average reference GS, and a lower dislocation density than in the other present orientations, associated with a slight decrease of the hardening rate. The next section will allow to interpret these reported mechanical data.

## **5. Modelling**

In order now to simulate the tensile tests, the polycrystalline samples are represented by their textures (orientation files obtained by XRD) and a viscoplastic Taylor type model is selected because of its numerical simplicity associated with its efficiency to simulate the behavior of a

polycrystalline sample represented by a large number of grains of various orientations [50].

The following boundary conditions are imposed to each grain, represented by its orientation

$$\dot{\boldsymbol{\epsilon}}_g = \begin{pmatrix} E_{11} & 0 & 0 \\ 0 & ? & 0 \\ 0 & 0 & ? \end{pmatrix} \quad \text{and} \quad \boldsymbol{\sigma}_g = \begin{pmatrix} ? & ? & ? \\ ? & 0 & ? \\ ? & ? & 0 \end{pmatrix} \quad (5)$$

In which the symbol ‘?’ indicates the non-imposed components, which can be deduced from the single crystal law defined in Eq. (6). In other words, a uniaxial tensile strain-rate along RD is imposed to each grain. We make use and build upon the dislocation-based crystal plasticity framework as initially proposed by Kocks and Mecking [27] for single crystals. We adopt a viscoplastic formulation for the flow rule which relates the shear strain rate  $\dot{\gamma}^s$  on a system  $s$  to the applied resolved shear stress  $\tau^s$  on the same system (and then the strain rate and stress at the level of the grain)

$$\dot{\gamma}^s = \dot{\gamma}_0 \left( \frac{\tau^s}{\tau_0^s} \right)^{1/m} \Rightarrow \quad \dot{\boldsymbol{\epsilon}}_g = \sum_s \dot{\gamma}^s \mathbf{R}_g^s = \sum_s \dot{\gamma}_0 \left( \frac{\boldsymbol{\sigma}_g \cdot \mathbf{R}_g^s}{\tau_0^s} \right)^{1/m} \mathbf{R}_g^s \quad (6)$$

where  $\tau_0^s$  is the so-called critical shear stress (CSS) of system  $s$ ,  $\dot{\gamma}_0$  is a reference strain rate,  $\mathbf{R}_g^s$  the orientation tensor of each system  $s$  within each grain  $g$  and  $m$  the strain-rate sensitivity exponent. Then, a generalized Taylor equation is adopted [51] to express  $\tau_0^s$  which reads

$$\tau_0^s = \mu b \sqrt{\sum a^{sl} \rho^l} \quad (7)$$

In this equation,  $a^{sl}$  measures the interaction strength between slip systems  $s$  and  $l$  with a dislocation density  $\rho^l$  on  $\tau_0^s$ . Due to crystal symmetries, the interaction matrix  $\mathbf{a}$  generally reduces to a limited number of interaction coefficients, *i.e.* three (maximum) for the forest interactions between non coplanar systems (Lomer-Cottrell locks, Hirth locks and glissile junctions), two for the weak interactions between systems gliding in parallel planes (self and coplanar interactions) and one for the colinear interactions [52, 53].

The dislocation equation is a generalization of the relation proposed initially by Kocks and Mecking [27] which describes the evolution rate of the total dislocation density with time for each slip system  $s$  as

$$\frac{d\rho^s}{dt} = \frac{1}{b} \cdot \left\{ \frac{\sqrt{\sum a^{sl}\rho^l}}{K} - 2 \left( \frac{\sum b^{sl}\rho^l}{\rho^s} \right) \rho^s \right\} \cdot |\dot{\gamma}|^s \quad (8)$$

The interactions between the moving dislocations on system  $s$  and the previously stored dislocations on other systems (and especially the orthogonal ones) contribute classically to the hardening of system  $s$  through the interaction matrix  $\mathbf{a}$ , but also to the softening of this system through what we call “indirect annihilation” [19] – represented here by the matrix  $\mathbf{b}$  – which we think is adequate to describe the specific softening mechanisms reported in Cube – oriented grains (e.g. [8]). The parameter  $K$  is directly linked to the dislocation mean free path.

Now, in general, different types of interactions can be considered for direct hardening ( $a^{sl}$  terms) and indirect annihilation ( $b^{sl}$  terms). In the present case, we use a general form for both matrices, but the coefficient corresponding to the Hirth locks (associated with orthogonal slip directions) is distinguished from coefficients associated with the other forest interactions and can be varied to modulate the influence of these locks on hardening. Some tensile tests have been performed with the parameters indicated in Table 7: the parameters composing the hardening matrix have been taken from Discrete Dislocation Dynamics simulations [52] and only the 4 parameters  $\rho_0$  (initial dislocation density on all systems),  $K$  (linked to the mean free path of dislocations),  $b_l$  (self interactions) and  $b_o$  (orthogonal interactions) have been adjusted on the experimental curves (see Fig. 14a). It is worth noting that in the present formulation, there is no explicit variation of  $\tau_0^s$  (and thus of the macroscopic stress) with grain size (see Eq. 7), as observed experimentally (see Fig.10). We thus assume that the selected initial  $\rho_0$  values *implicitly* not only account for possible initial different dislocation densities within the samples (which are not expected in the present case after the performed annealing treatments), but also *implicitly* account for initial different grain sizes as experimentally

observed. It is also worth noting that one single set of hardening and softening parameters allows reproducing satisfactorily the 4 experimental curves (both in terms of stress level and hardening evolution), corresponding to different textures and initial grain sizes (solely represented by different  $\tau_0$  values). The comparison of the experimental hardening rates with the simulated hardening rates is presented in Fig. 14b for the two extreme cases regarding the Cube percentage. It is clear from this figure that the experimental hardening rate is indeed constant over an important portion of the tensile curve for the (73% CR – Annealed at 350°C) sample, whereas it decreases constantly for the (96% CR – Annealed at 200°C) sample. This difference is satisfactorily reproduced by the model, which thus confirms the decrease of the hardening rate at large strains for the (96% CR – Annealed at 200°C) sample, which contains a high percentage of Cube component.

Additionally, the average dislocation densities obtained at the end of the simulations for the main texture components (taken as single orientations and not scattered texture components in this case to illustrate the sole effect of orientation and not that of the texture dispersion) as well as for the whole polycrystal have also been extracted from the simulations and are reported in Table 6. All measured and estimated values of dislocation density are graphically represented in Fig. 15. The difference between the two main components, already observed experimentally and discussed in Section 4, is reproduced by the model for the 96%CR and annealed sample, although the predicted values are larger than the XRD or GND measured values. It has to be remembered though that the individual predicted density values are extracted from a simulation which does not take into account an explicit Hall-Petch effect on the initial CSS. The predicted textures, using the adjusted parameters and the initial experimental textures are shown in Fig. 16. It is seen that the agreement with the measured ones is quite good, thus validating the use of the selected simple model to investigate the behavior of some specific orientations. Indeed, this model is able to reproduce simultaneously

the macroscopic behavior as well as the texture evolution of several samples differing by their initial texture and microstructure. A more advanced approach, such as the use of a self-consistent model [54] or a FE simulation [31], based on the very same single crystal constitutive law, would probably still improve the predictive capacity of the simulations; this improvement is however expected to be small at such moderate strains.

## 6. Discussion

A close inspection of the complete set of experimental (Section 3 and 4) and numerical (Section 5) results and of the data listed in Table 6 call for the following comments:

- From the simulations, we can say that recovery is strongly active in the present tensile experiments in the Cube orientation, just like in rolling: in fact, in the performed simulations, 8 systems are active at the very beginning of simulation, but due to the specific shape of the hardening law, the number of active systems goes down to 4 at the end of the calculation. As expected, the Cube orientation is predicted to be stable in tension, and thus no subgrain boundaries, constituted of GNDs and associated with rather large misorientations are expected to form; this is consistent with the KAM map shown in Fig. 13.
- Recovery is also active within the CubeT oriented grains, but to a much lower extent (see the final predicted densities in Table 6); in this case, the number of active systems fluctuates during the simulation because of reorientation. Also, as this orientation is unstable in tension, we expect an increase of the GND density due some fragmentation of the grains during reorientation. Indeed, the measured  $\rho_{GND}$  is always higher in the CubeT orientation than in the Cube one, and fragmentation of this orientation is clearly observed experimentally (Fig. 13).

The model used here, while very simple, is thus able to reproduce satisfactorily the macroscopic curves and global textures and at least qualitatively, the observed differences in terms of dislocation densities within individual components. However, the GS effect on the yield stress (see Fig. 10) was unexpected and this is why simple relations neglecting the GS influence between stress and dislocation densities were used both for the macroscopic stress (Eq. 4) and the CSS (Eq. 7). Also, even if the simulations predict an enhanced recovery within the Cube orientated grains, compared to all other textures orientations, it is not clear at this stage that it is completely responsible for the decrease of the macroscopic hardening rate observed for the samples containing a high percentage of Cube. In order thus to separate the texture and microstructure effects on hardening, the 4 experimental curves have again been simulated with the hardening and softening parameters listed in Table 7, but the initial dislocation density on each slip system has been imposed to be the same for all cases ( $\rho_0 = 6 \cdot 10^{12} \text{m}^{-2}$ ), and has been forced to remain constant during the simulation. In other words, microstructural hardening has been suppressed from the simulation. The results of such simulations are presented in Fig. 17, where both tensile stress – strain curves and hardening curves are represented. It is seen that the evolution of stress due to the sole texture evolution is indeed quite limited; during the simulation, as the texture tends to stabilize, the hardening rate due to texture reorientation tends to decrease (see Fig. 17b), and this decrease occurs sooner for textures containing a higher percentage of Cube, since this main component is stable in tension. As a result, the curves corresponding to the (93% CR – Annealed at 250°C) and (96% CR – Annealed at 200°C) samples do present a slight parabolic shape (see Fig. 17a), just like the experimental curves. In other words, we do have for these samples, an overall decrease of the hardening rate, associated with a significant textural decrease of the hardening rate, and a microstructural decrease of the hardening rate due to enhanced recovery

of the dislocation microstructures in the Cube oriented grains. Both sets of simulated curves can help to quantify these two components. Indeed, we can rewrite Eq. (4) as

$$\sigma(\varepsilon) = M(\varepsilon)\tau(\varepsilon) \quad (9)$$

In which  $\tau(\varepsilon)$  is simply defined as  $\sigma(\varepsilon)/M(\varepsilon)$  and evolves with the dislocation density.

Deriving this equation with strain gives

$$\frac{d\sigma}{d\varepsilon} = M(\varepsilon)\frac{d\tau}{d\varepsilon} + \tau(\varepsilon)\frac{dM}{d\varepsilon} = \frac{d\sigma}{d\varepsilon}(\text{microstructure}) + \frac{d\sigma}{d\varepsilon}(\text{texture}) \quad (10)$$

The hardening rate is thus composed of two terms, one due to the evolution of the dislocation densities on all slip systems (the microstructural hardening component) and the other due to texture evolution (the textural hardening component). The total variations of  $\sigma$  and  $M$  over the whole tensile tests can be estimated from the simulations presented in Fig. 14 (for  $\sigma$ ) and 17 (for  $M$ ) which in turn allow to evaluate the variation of  $\tau$ . If we then also extract from the simulations average values of  $M$  and  $\tau$  over the whole tensile test, we can estimate the two parts of Eq. (10). For the two extreme cases (73% CR – Annealed at 350°C) and (96% CR – Annealed at 200°C), we find that  $\frac{\Delta\sigma}{\Delta\varepsilon}(\text{texture}) \cong 10$  MPa, whereas  $\frac{\Delta\sigma}{\Delta\varepsilon}(\text{microstructure}) \cong 219$  and 204 MPa for the two cases. In other words, the microstructural component of hardening is always much larger than the textural component. Additionally, we observe a decrease of the textural hardening component in all cases, which starts at  $\varepsilon \cong 0.07$  for the sample containing the highest Cube percentage and only at  $\varepsilon \cong 0.17$  for the texture containing the lowest Cube percentage. It does not affect the global hardening curve in this last case. As for the (96%CR – Annealed at 200°C) sample, the hardening and softening (including enhanced recovery in the Cube orientation) mechanisms occurring within individual grains also contribute to a much larger extent to the observed variation of hardening rate than the texture stabilization.

It could also be argued at this point, that the fact that the amount of recovery (or more precisely of “indirect annihilation”) within the main texture components varies with

orientation in accordance with the measured dislocation densities could simply be due to the identification procedure, and that a similar result could as well be obtained without considering anisotropic softening. Indeed, if we adopt the more classical formulation for the evolution of dislocation density, which comprises one single recovery parameter  $y_c$  (i.e. “isotropic” recovery)

$$\frac{d\rho^s}{dt} = \frac{1}{b} \cdot \left\{ \frac{\sqrt{\sum a^{sl} \rho^l}}{K} - 2y_c \rho^s \right\} \cdot |\dot{\gamma}|^s \quad (11)$$

and vary the value of  $y_c$  to enhance recovery, we do observe different hardening / softening behaviors for the two main individual orientations. This is illustrated in Fig. 18, in which the behavior of the two Cube and CubeT orientations is presented for different sets of hardening and softening (see Table 8). It is seen that, by imposing an enhanced isotropic recovery in the two orientations, a parabolic curve can indeed be found for individual components, but softening becomes then much more important in the CubeT orientation than in the Cube one, in total contradiction with the measurements presented above. As a result, we failed at reproducing simultaneously the four experimental curves with one single set of parameters with this more simple law. This has indeed already been noticed by other researchers, who performed finite elements (FE) simulations with an even simpler dislocation-based hardening law (with no distinct interactions terms between systems for hardening or softening) and were obliged to select different parameters for different tensile axes [3]. Although a complete investigation of the influence of all parameters on the behavior of individual orientations has not been done here (since we think that, even with a simple model as the selected one, it is out of reach), the present simulations thus show clearly that the observed macroscopic behaviors are indeed simultaneously reproduced by considering *anisotropic* softening. This observation is in agreement with some recent finite element (FE) simulations performed on aluminum, which made use of a quite complex single crystal constitutive law comprising also an anisotropic recovery term [55, 56]. This last constitutive law seems however difficult to

completely justify experimentally, since it distinguishes between edge and screw dislocations (only the screw dislocation density rate contains an anisotropic recovery term) and may thus contain more adjustable parameters than the one proposed in the present case (at least 2 more). Nevertheless, like in the present simulations, these authors were able to reproduce several tensile curves (for Al single crystals) with one single set of parameters.

Finally, because of the unexpected Hall-Petch effect of the Cube texture, we can propose a modification of the general Taylor hardening law (Eq. 4), which can be rewritten, as often proposed in the literature, as

$$\sigma(\varepsilon) = \sigma(d_M, \rho_M) = \sigma(d_M) + M(\varepsilon)\alpha\mu b\sqrt{\rho_M(\varepsilon)} \quad (12)$$

By assuming that the XRD determination does give a good estimate of  $\rho_M$ , this can be rewritten as

$$\sigma(\varepsilon) = \sigma(d_M) + M(\varepsilon)\alpha\mu b\sqrt{\rho_{XRD}(\varepsilon)} \quad (13)$$

If we consider now that the term  $\sigma(d_M)$ , which explicitly accounts for the influence of the average grain size on yield stress, does not evolve much with strain, we can also write the yield stress as

$$\sigma_0 = \sigma(d_M) + M(\varepsilon = 0)\alpha\mu b\sqrt{\rho_M(\varepsilon = 0)} \quad (14)$$

which allows to evaluate the macroscopic initial density. By doing so for the two extreme samples, we find that the macroscopic initial dislocation density is equal to  $5.10^{12} \text{ m}^{-2}$  for the (73% CR – Annealed at 350°C) sample and to  $3.10^{12} \text{ m}^{-2}$  for the (96% CR – Annealed at 200°C) sample. These values are consistent with the one measured on the undeformed Cu single crystal presented in Fig.12 and confirm the fact that these samples were initially completely recrystallized. In the performed simulations performed without explicit influence on the GS on the yield stress, the adjusted macroscopic dislocation densities were equal to  $12.10^{12} \text{ m}^{-2}$  for the (73% CR – Annealed at 350°C) sample and  $72.10^{12} \text{ m}^{-2}$  for the (96% CR – Annealed at 200°C) sample. Thus, from the comparison between the initial dislocation

densities obtained with or without an explicit GS term in the yield stress expression, we notice again that the GS effect is more important for the sample containing the largest proportion of the Cube orientation. Due to the observed (both experimentally and numerically) large increase of the dislocation densities during tensile deformation, we suspect though that this difference will then drastically decrease with strain and that the final estimated dislocation densities in the present work are thus still valid ; this will be checked in future work.

## **7. Conclusions**

We report experimental (microstructural and mechanical) data in the present work, concerning the influence of the Cube component on the mechanical behavior of copper samples deformed in tension. These data have been compared with some simulations performed with a simple Taylor type model taking into account a dislocation-based hardening law containing both anisotropic hardening and softening terms, in order to characterize the behavior of individual components. The major conclusions of this work are the following:

- A high percentage of Cube oriented grains does not necessarily produces a softer material, as expected from the sole orientation effect; the grain size distribution plays also an important role on the initial strength of the tested materials. In the present case, the grain size evolves as a result of two different recrystallization mechanisms, which are nucleation and growth of new grains and twinning;
- The spread observed in the grain size distributions, partly due to the occurrence of twinning during annealing performed before deformation in tension, has to be taken into account to reproduce a Hall- Petch type hardening effect;

- The Cube orientation is associated with a lower dislocation density after 25% tension than any other orientation; both GND density (as measured from EBSD) and total dislocation density (as measured by XRD) are indeed lower in this orientation;
- The proposed hardening / softening law allows to *simultaneously* reproducing all experimental curves with one single set of hardening / softening parameters. Only the initial value of dislocation density needs to be varied for the different samples, since it indirectly accounts for the variation in the initial grain size of these samples; it is thus particularly well adapted to samples which do not present too strong variations in grain size;
- The performed simulations demonstrate that dynamic recovery is indeed more active in the Cube orientation than in the other present orientations, due to the specific dislocation microstructure which forms during straining, resulting from the activation of orthogonal systems;
- By incorporating into the Taylor equation which describes the evolution of stress with dislocation density, an additional term which depends on the initial grain size of the material, it has also been possible to estimate the initial dislocation density of some samples. The values of densities estimated by XRD for undeformed or deformed samples are in very good agreement with previously published data on copper, or with values estimated from EBSD. This observation tends to prove that our XRD measurements and analysis are highly reliable.
- The effect of recovery within the Cube component on the hardening behavior of the material may however be considered to be quite limited, compared e.g. to the influence of the same orientation on the anisotropic deformation during metal forming [57]. But, as it concerns in the present case, one single tensile direction and a moderate total strain it is expected to become more important if these two features are changed.

Also, these conclusions have been drawn from measurements performed at the macroscopic scale (tensile curves) and mesoscopic scale (that of individual grains or texture components). It could be interesting now to see if it is possible to bring some additional proofs by observing or simulating the same hardening and softening phenomena at a lower scale, like e.g. that of the dislocation microstructure through Transmission Electronic Microscopy (TEM) measurements or Discrete Dislocation Dynamics (DDD) simulations. Finally, as the observations performed here in copper can have important technological consequences (like the general control of the anisotropy of the material during metal forming), it could be interesting to perform the same kinds of observations in other FCC metals of industrial interest, like the Al or Ni alloys. This is planned in some future works.

### **Acknowledgments**

The help of B. Djiba, O. Brinza and A. Hocini, from LSPM, as well as the participation of F. Feuillette and A. Lam (former master students) in obtaining some of the experimental data presented here is gratefully acknowledged. ANR (Agence Nationale de la Recherche) and CGI (Commissariat à l'Investissement d'Avenir) are gratefully acknowledged for their financial support through Labex SEAM (Science and Engineering for Advanced Materials and devices), ANR 11 LABX 086, ANR 11 IDEX 05 02.

### **References**

1. Gerber, P., J. Tarasiuk, T. Chauveau, and B. Bacroix, *A quantitative analysis of the evolution of texture and stored energy during annealing of cold rolled copper*. Acta Materialia, 2003. **51**(20): p. 6359-6371.

2. Mecif, A., B. Bacroix, and P. Franciosi, *Temperature and orientation dependent plasticity features of Cu and Al single crystals under axial compression—I. Lattice rotation effects and true hardening stages*. Acta Materialia, 1997. **45**(1): p. 371-381.
3. Lee, M.G., H. Lim, B.L. Adams, J.P. Hirth, and R.H. Wagoner, *A dislocation density-based single crystal constitutive equation*. International Journal of Plasticity, 2010. **26**(7): p. 925-938.
4. Mohamed, G. and B. Bacroix, *Role of stored energy in static recrystallization of cold rolled copper single and multicrystals*. Acta Materialia, 2000. **48**(13): p. 3295-3302.
5. Piekos, K., J. Tarasiuk, K. Wierzbanski, and B. Bacroix, *Generalized vertex model of recrystallization - Application to polycrystalline copper*. Computational Materials Science, 2008. **42**(4): p. 584-594.
6. Hirsch, J. and K. Lücke, *Overview no. 76: Mechanism of deformation and development of rolling textures in polycrystalline f.c.c. metals—I. Description of rolling texture development in homogeneous CuZn alloys*. Acta Metallurgica, 1988. **36**(11): p. 2863-2882.
7. Kallend, J. and Y. Huang, *Orientation dependence of stored energy of cold work in 50% cold rolled copper*. Metal science, 1984. **18**(7): p. 381-386.
8. Ridha, A.A. and W.B. Hutchinson, *Recrystallisation mechanisms and the origin of cube texture in copper*. Acta Metallurgica, 1982. **30**(10): p. 1929-1939.
9. Saimoto, S., W.F. Hosford Jr, and W.A. Backofen, *Slip in twinned copper crystals*. Acta Metallurgica, 1965. **13**(10): p. 1086-1088.
10. Tarasiuk, J., B. Bacroix, K. Wierzbanski, S. Wronski, and P. Gerber, *Room temperature recovery in rolled polycrystalline copper after many years*, in *Recrystallization and Grain Growth Iv*, E.J. Palmiere and B.P. Wynne, Editors. 2012. p. 758-763.
11. Borbély, A., G. Hoffmann, E. Aernoudt, and T. Ungár, *Dislocation arrangement and residual long-range internal stresses in copper single crystals at large deformations*. Acta Materialia, 1997. **45**(1): p. 89-98.

12. Huang, X., J.J. D., and N. Hansen. *Effect of grain orientation on deformation structure and recrystallization behavior of tensile strained copper*. in *4th International Conference on Recrystallization and Related Phenomena*. 1999. Tsukuba City, Japan: JIM.
13. Jiang, J., T.B. Britton, and A.J. Wilkinson, *Evolution of dislocation density distributions in copper during tensile deformation*. *Acta Materialia*, 2013. **61**(19): p. 7227-7239.
14. Fattah-Alhosseini, A., O. Imantalab, Y. Mazaheri, and M.K. Keshavarz, *Microstructural evolution, mechanical properties, and strain hardening behavior of ultrafine grained commercial pure copper during the accumulative roll bonding process*. *Materials Science and Engineering: A*, 2016. **650**: p. 8-14.
15. Gu, C.F., L.S. Tóth, and B. Beausir, *Modeling of large strain hardening during grain refinement*. *Scripta Materialia*, 2012. **66**(5): p. 250-253.
16. Wang, J.-l., R.-d. Xu, S.-h. Wang, T.-c. Qian, and Q.-n. Shi, *Formation mechanism and organizational controlling of ultra-fine-grain copper processed by asymmetrical accumulative rolling-bond and annealing*. *Transactions of Nonferrous Metals Society of China*, 2012. **22**(11): p. 2672-2678.
17. Lebensohn, R.A., R. Brenner, O. Castelnau, and A.D. Rollett, *Orientation image-based micromechanical modelling of subgrain texture evolution in polycrystalline copper*. *Acta Materialia*, 2008. **56**(15): p. 3914-3926.
18. Hug, E., P.A. Dubos, and C. Keller, *Temperature dependence and size effects on strain hardening mechanisms in copper polycrystals*. *Materials Science and Engineering: A*, 2013. **574**(0): p. 253-261.
19. Bacroix, B. and R. Brenner, *A phenomenological anisotropic description for dislocation storage and recovery processes in fcc crystals*. *Computational Materials Science*, 2012. **54**: p. 97-100.
20. Gerard, C., G. Cailletaud, and B. Bacroix, *Modeling of latent hardening produced by complex loading paths in FCC alloys*. *International Journal of Plasticity*, 2013. **42**: p. 194-212.
21. Gracio, J.J., *The double effect of grain size on the work hardening behaviour of polycrystalline copper*. *Scripta Metallurgica et Materialia*, 1994. **31**(4): p. 487-489.

22. Jia, N., X. Zhao, D. Song, M.H. Zhou, and Y.D. Wang, *On the anomalous hardening during annealing of heavily deformed f.c.c. metals*. Materials Science and Engineering: A, 2010. **527**(4–5): p. 1143-1150.
23. Mohamed, G., B. Bacroix, T. Ungar, J.L. Raphanel, and T. Chauveau, *Experimental and numerical determination of the intragranular work hardening in a cold rolled polycrystal*. Materials Science and Engineering: A, 1997. **234–236**: p. 940-943.
24. Wiecek, N., G. Laplanche, J.K. Heyer, A.B. Parsa, J. Pfetsching-Micklich, and G. Eggeler, *Assessment of strain hardening in copper single crystals using in situ SEM microshear experiments*. Acta Materialia, 2016. **113**: p. 320-334.
25. Sinclair, C.W., W.J. Poole, and Y. Bréchet, *A model for the grain size dependent work hardening of copper*. Scripta Materialia, 2006. **55**(8): p. 739-742.
26. Takeuchi, T., *Work Hardening of Copper Single Crystals with Multiple Glide Orientations*. Transactions of the Japan Institute of Metals, 1975. **16**(10): p. 629-640.
27. Kocks, U.F. and H. Mecking, *Physics and phenomenology of strain hardening: the FCC case*. Progress in Materials Science, 2003. **48**(3): p. 171-273.
28. Hosford Jr, W.F., R.L. Fleischer, and W.A. Backofen, *Tensile deformation of aluminum single crystals at low temperatures*. Acta Metallurgica, 1960. **8**(3): p. 187-199.
29. Hutchinson, B., *The Cube Texture Revisited*. Materials Science Forum, 2012. **702-703**: p. 3-10.
30. Pawlik, K., *Determination of the Orientation Distribution Function from Pole Figures in Arbitrarily Defined Cells*. Phys.Stat.Sol.(b) 1986. **134**: p. 477.
31. Chiron, R., J. Fryet, and P. Viaris de Lesegno, *Device for SEM and EBSD in situ tensile tests up to 800°C*, in *International Symposium on Local Strain and Temperature Measurements in non-uniform fields at elevated temperatures*, 1996: Berlin, Germany.
32. Wang, W., F. Brisset, A.L. Helbert, D. Solas, I. Drouelle, M.H. Mathon, and T. Baudin, *Influence of stored energy on twin formation during primary recrystallization*. Materials Science and Engineering: A, 2014. **589**: p. 112-118.

33. Kumar, M., A.J. Schwartz, and W.E. King, *Microstructural evolution during grain boundary engineering of low to medium stacking fault energy fcc materials*. Acta Materialia, 2002. **50**(10): p. 2599-2612.
34. Woldt, E. and D.J. Jensen, *Recrystallization kinetics in copper: Comparison between techniques*. Metallurgical and Materials Transactions A, 1995. **26**(7): p. 1717-1724.
35. Baudin, T., A.L. Etter, and R. Penelle, *Annealing twin formation and recrystallization study of cold-drawn copper wires from EBSD measurements*. Materials Characterization, 2007. **58**(10): p. 947-952.
36. Zhang, S., J. Zhou, L. Wang, and Y. Wang, *The effect of the angle between loading axis and twin boundary on the mechanical behaviors of nanotwinned materials*. Materials & Design, 2013. **45**: p. 292-299.
37. Berbenni, S., V. Favier, and M. Berveiller, *Impact of the grain size distribution on the yield stress of heterogeneous materials*. International Journal of Plasticity, 2007. **23**(1): p. 114-142.
38. Raesinia, B. and C.W. Sinclair, *A representative grain size for the mechanical response of polycrystals*. Mater. Sci. Eng. A, 2009. **525**: p. 78-82.
39. Hansen, N., *Boundary strengthening in undeformed and deformed polycrystals*. Materials Science and Engineering: A, 2005. **409**(1-2): p. 39-45.
40. Wauthier-Monnin, A., T. Chauveau, O. Castelnau, H. Réglé, and B. Bacroix, *The evolution with strain of the stored energy in different texture components of cold-rolled IF steel revealed by high resolution X-ray diffraction*. Materials Characterization, 2015. **104**(0): p. 31-41.
41. Groma, I., T. Ungar, and M. Wilkens, *Asymmetric X-Ray line broadening of plastically deformed crystals. 1. Theory*. Journal of Applied Crystallography, 1988. **21**: p. 47-53.
42. Ungár, T., I. Dragomir, A. Révész, and A. Borbély, *The contrast factors of dislocations in cubic crystals: the dislocation model of strain anisotropy in practice*. Journal of Applied Crystallography, 1999. **32**: p. 992-1002
43. Ungar, T., J. Gubicza, G. Ribarik, and A. Borbély, *Crystallite size distribution and dislocation structure determined by diffraction profile analysis: principles and practical application to cubic and hexagonal crystals*. Journal of Applied Crystallography, 2001. **34**: p. 298-310.

44. Konijnenberg, P.J., S. Zaefferer, and D. Raabe, *Assessment of geometrically necessary dislocation levels derived by 3D EBSD*. Acta Materialia, 2015. **99**: p. 402-414.
45. Nye, J.F., *Some geometrical relations in dislocated crystals*. Acta Metallurgica, 1953. **1**(2): p. 153-162.
46. Moussa, C., M. Bernacki, R. Besnard, and N. Bozzolo, *About quantitative EBSD analysis of deformation and recovery substructures in pure Tantalum*. IOP Conf. Ser. Mater. Sci. Eng. 89 2015: p. 12038.
47. Moussa, C., M. Bernacki, R. Besnard, and N. Bozzolo, *Statistical analysis of dislocations and dislocation boundaries from EBSD data*. Ultramicroscopy, 2017. **179**: p. 63-72.
48. Devincere, B., L. Kubin, and T. Hoc, *Physical analyses of crystal plasticity by DD simulations*. Scripta Materialia, 2006. **54**(5): p. 741-746.
49. Siv, E., *Etude de la migration des joints dans le cuivre*, PhD thesis, 2018, Paris 13 University.
50. Ma, A., F. Roters, and D. Raabe, *Numerical study of textures and Lankford values for FCC polycrystals by use of a modified Taylor model*. Computational Materials Science, 2004. **29**(3): p. 353-361.
51. Franciosi, P. and A. Zaoui, *Multislip in f.c.c. crystals a theoretical approach compared with experimental data*. Acta Metallurgica, 1982. **30**(8): p. 1627-1637.
52. Kubin, L., B. Devincere, and T. Hoc, *Modeling dislocation storage rates and mean free paths in face-centered cubic crystals*. Acta Materialia, 2008. **56**(20): p. 6040-6049.
53. Franciosi, P., M. Berveiller, and A. Zaoui, *Latent hardening in copper and aluminium single crystals*. Acta Metallurgica, 1980. **28**(3): p. 273-283.
54. Brenner, R., O. Castelnau, and B. Bacroix, *Potentiality of mean-field approaches for recrystallisation: characterization of the deformed state of polycrystals*, in *Recrystallization and Grain Growth, Pts 1 and 2*, B. Bacroix, et al., Editors. 2004. p. 33-38.
55. Cheong, K.-S. and E.P. Busso, *Discrete dislocation density modelling of single phase FCC polycrystal aggregates*. Acta Materialia, 2004. **52**(19): p. 5665-5675.

56. Ha, S., J.-H. Jang, and K. Kim, *Finite element implementation of dislocation-density-based crystal plasticity model and its application to pure aluminum crystalline materials*. International Journal of Mechanical Sciences, 2017. **120**: p. 249-262.
57. Bacroix, B. and P. Gilormini, *Finite-element simulations of earing in polycrystalline materials using a texture-adjusted strain-rate potential*. Modelling and Simulation in Materials Science and Engineering, 1995. **3**(1): p. 1-21.

Table 1. Selected annealing temperatures for each rolling reduction (annealing time = 15 min).

Rolling Reduction before annealing (%)	73	84	93	96
Annealing Temperature for full recrystallization (°C)	350	300	250	200

Table 2. Microstructural parameters extracted from the EBSD maps.

Rolling Reduction (%) before annealing	% Cube after annealing		Average GS (equ. diameter in $\mu\text{m}$ )	Standard Deviation (equ. diameter in $\mu\text{m}$ )	Area-weighted average GS (equ. diameter in $\mu\text{m}$ )	Representative grain size (equ. diameter in $\mu\text{m}$ )	% TB $60^\circ <111>$	% GB between $58^\circ$ and $62^\circ$	% GB between $15^\circ$ and $58^\circ$
	EBSD	DRX							
73	4	4	2.45	3.24	12.86	18.14	57.0	58.8	30
84	7	5	2.70	2.87	9.57	13.23	63.2	64.8	33
93	16	15	2.49	2.60	8.64	10.87	58.4	59.3	35
96	37	37	2.37	2.77	10.73	10.32	54.2	55.5	33

Table 3. Calculated percentages of the orientations Cube and CubeT before and after 25% strain.

Thermomechanical Treatment before tension	Orientation	% before tension (after annealing)	% after tension
73% CR – Annealing at $350^\circ\text{C}$ (15 min)	Cube	4.06	5.07
	CubeT	9.36	8.91
96% CR – Annealing at $200^\circ\text{C}$ (15 min)	Cube	36.39	51.17
	CubeT	18.39	12.89

Table 4. Predicted Taylor Factors before and after tension (at 25% strain), using the boundary conditions described by Equation (5).

Thermomechanical Treatment before tension	Initial Taylor Factor (before tension)	Final Taylor Factor (at 25% tensile strain)
73% CR – Annealing at $350^\circ\text{C}$	2.76	2.94
84% CR – Annealing at $300^\circ\text{C}$	2.80	2.98
93% CR – Annealing at $250^\circ\text{C}$	2.80	2.96
96% CR – Annealing at $200^\circ\text{C}$	2.72	2.87

Table 5. Crystallographic parameters for all peaks considered in the measurements of the dislocation densities.

Diffracting planes	{111}	{200}	{220}	{222}	{311}
$2\theta$ values ( $^\circ$ )	51.00	59.62	89.34	102.00	111.05
K ( $\text{nm}^{-1}$ )	4.8129332	5.5576551	7.5897112	8.6881653	9.2163284

Table 6. Dislocations densities for individual texture components extracted from the X-Ray peaks ( $\rho_{XRD}$ ), the EBSD maps ( $\rho_{gnd}$ ) and from the simulations ( $\rho_{pred.}$ ), after tension ( $\epsilon=0.25$ ). The polycrystalline values ( $\rho_M$ ) estimated from the tensile curves are also indicated. The values (in  $m^{-2}$ ) have to be multiplied by  $10^{14}$ .

Orientation	73% CR and annealed				96% CR and annealed			
	$\rho_{XRD}$	$\rho_{gnd}$ (KAM)	$\rho_M$	$\rho_{pred.}$	$\rho_{XRD}$	$\rho_{gnd}$ (KAM)	$\rho_M$	$\rho_{pred.}$
Cube	4.6	3.12		2.51	3.4	3.06		4.07
CubeT	4.5	3.36		9.12	5.6	5.10		11.7
Polycrystal		4.86	5.11	6.20		5.04	6.90	7.42

Table 7. The parameter sets considered for the four polycrystalline simulations performed in tension and presented in Fig. 14.

Case	$\rho_0$	$K$	$b_1$	$b_2$	$b_3$	$b_4$	$b_5$
	( $10^{12} m^{-2}$ )		(x $10^{-9}$ )				
73% CR, annealed	1	15	1.5	0	0	1.0	0
84% CR, annealed	4						
93% CR, annealed	6						
96% CR, annealed							
$1/m = 51$ , $\mu = 45000$ , $b = 2.56 \cdot 10^{-10}$ m, $a_1 = a_2 = a_5 = 0.122$ , $a_3 = 0.625$ , $a_4 = 0.07$							

Indices correspond to the following interactions: 1=self, 2=coplanar, 3=collinear, 4=orthogonal (Hirth locks) and 5 = others (Lomer – Cottrell locks and glissile junctions).

Table 8. The parameter sets considered for the simulations performed for individual texture components and presented in Fig. 17.

Case	$\rho_0$	$K$	$b_1$	$b_2$	$b_3$	$b_4$	$b_5$
	(x $10^{12}$ )		(x $10^{-9}$ )				
Classical Isotropic Recovery	6	15	2.5	0	0	0.0	0
Enhanced Isotropic Recovery	6	15	5.0	0	0	0.0	0
Anisotropic recovery	6	15	1.5	0	0	1.0	0
$1/m = 51$ , $\mu = 45000$ , $b = 2.56 \cdot 10^{-10}$ m, $a_1 = a_2 = a_5 = 0.122$ , $a_3 = 0.625$ , $a_4 = 0.07$							

Indices correspond to the interactions: 1=self, 2=coplanar, 3=collinear, 4=orthogonal and 5 = others.

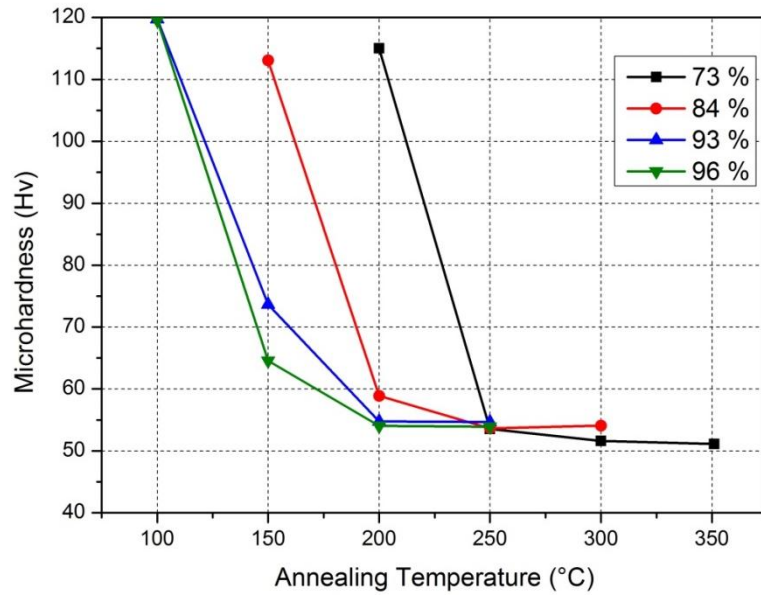


Fig. 1. Evolution of the microhardness as a function of the annealing temperature for a constant annealing time of 15 min, for the samples rolled at various rolling reductions between 73 and 96%.

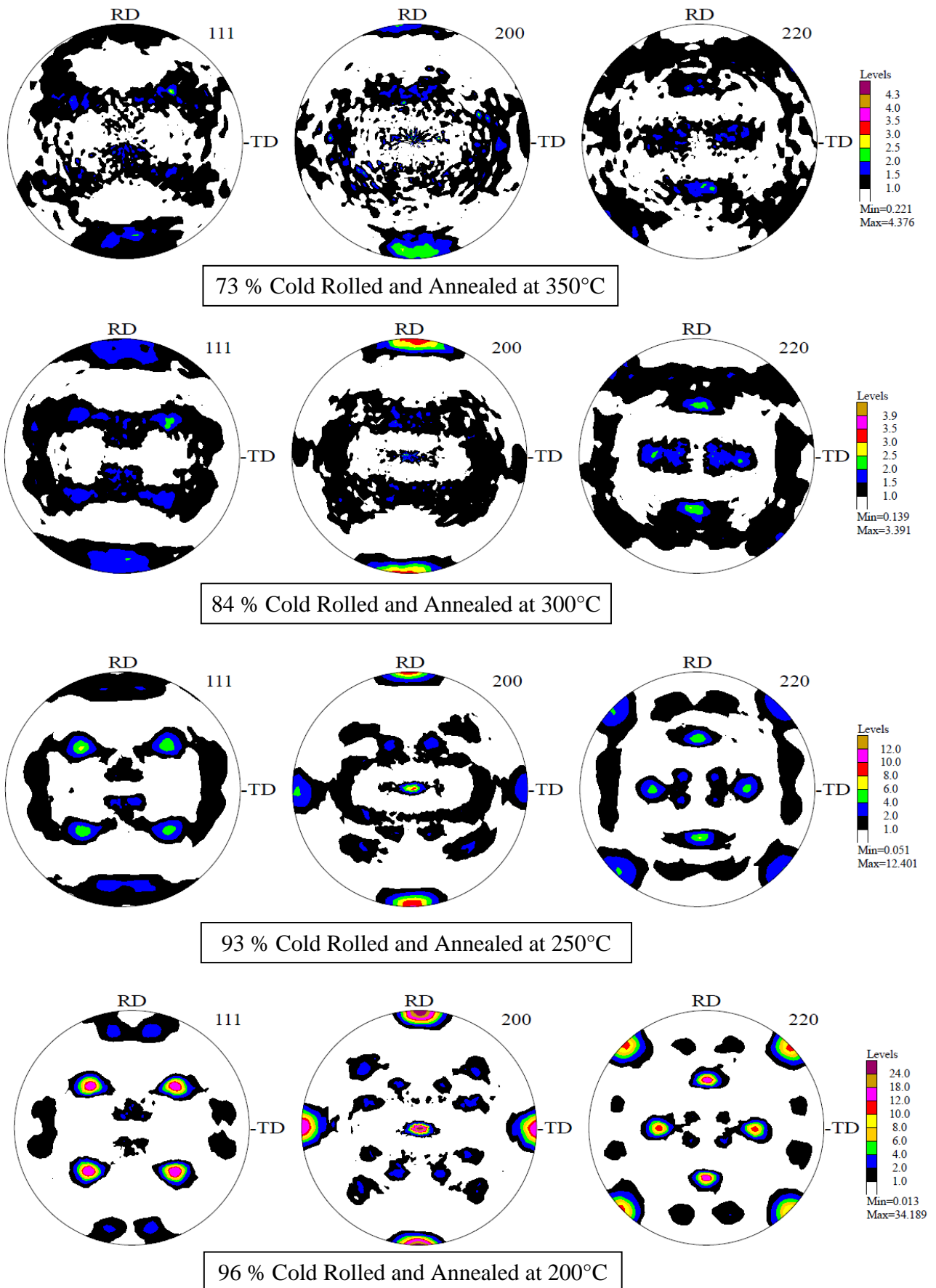


Fig. 2.  $(111)$ ,  $(200)$  and  $(220)$  recalculated pole figures, measured by X-ray diffraction after different amounts of cold – rolling, followed by a heat-treatment inducing full recrystallization.

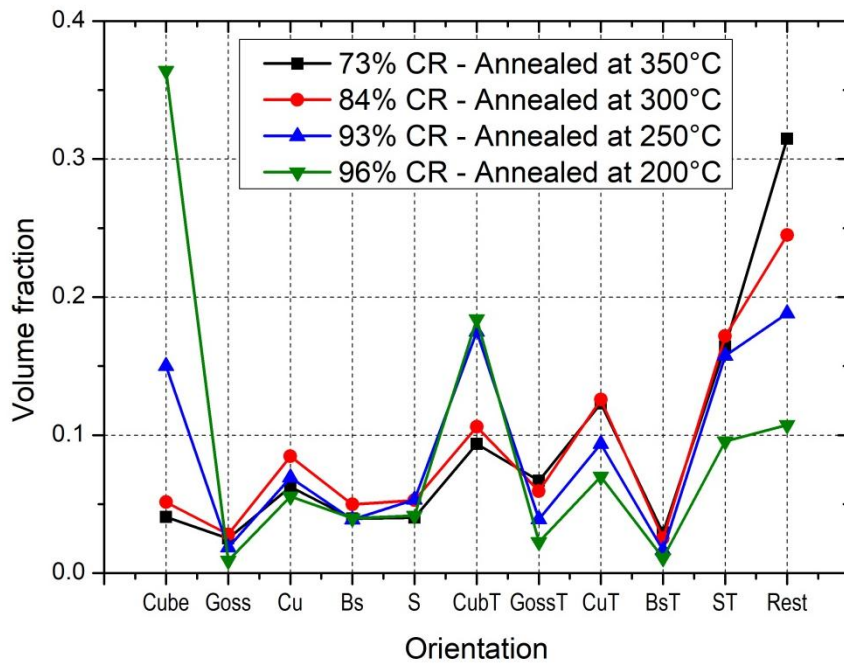


Fig. 3. Calculated volume fractions from the XRD measurements of the principal texture components and associated twin components classically composing the rolled and annealing copper textures. The symmetrical orientations (due to the orthotropy of the rolling process) are grouped, as well as the different twin orientations associated with one given orientation. Rest is composed of all remaining orientations present in the texture which are not closed to one of the 50 orientations of interest.

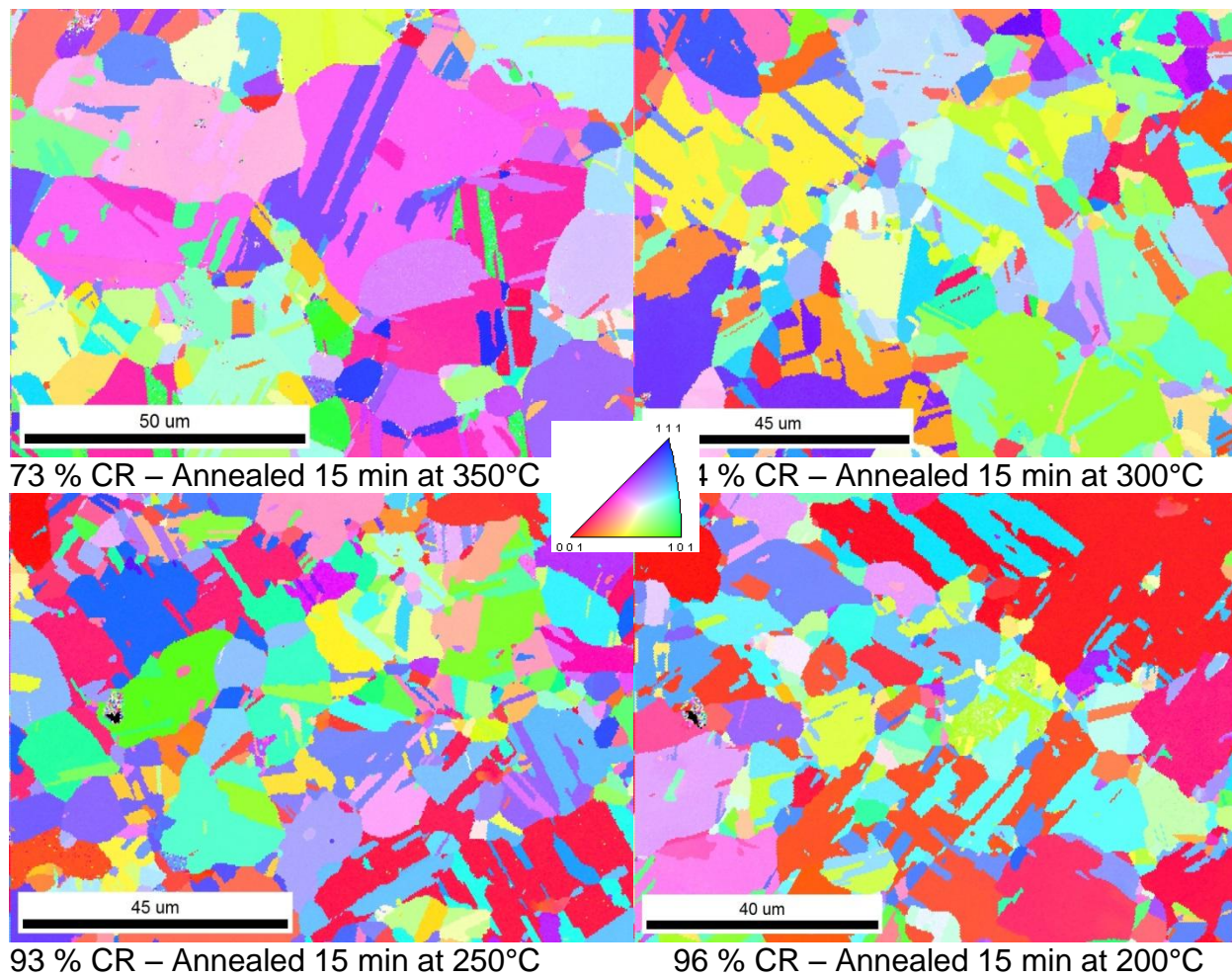


Fig. 4. Typical EBSD orientations maps obtained for the 4 investigated materials. The color indicates the orientation of the rolling direction of the sample, according to the color code indicated by the small triangle. The step size is 0.3  $\mu\text{m}$ .

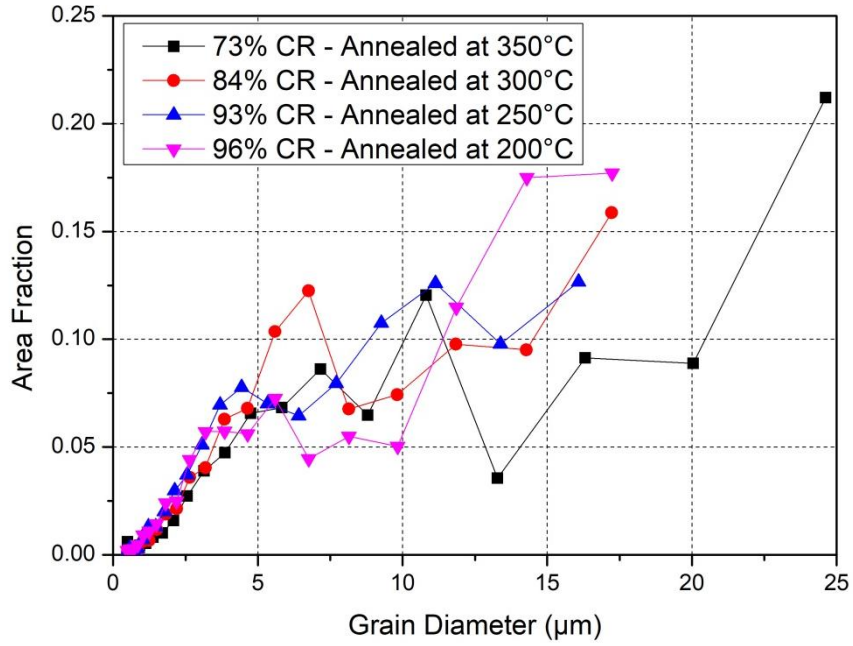


Fig. 5. Grain size distributions for the 4 investigated materials. The grain size is represented here by an equivalent diameter (in  $\mu\text{m}$ ).

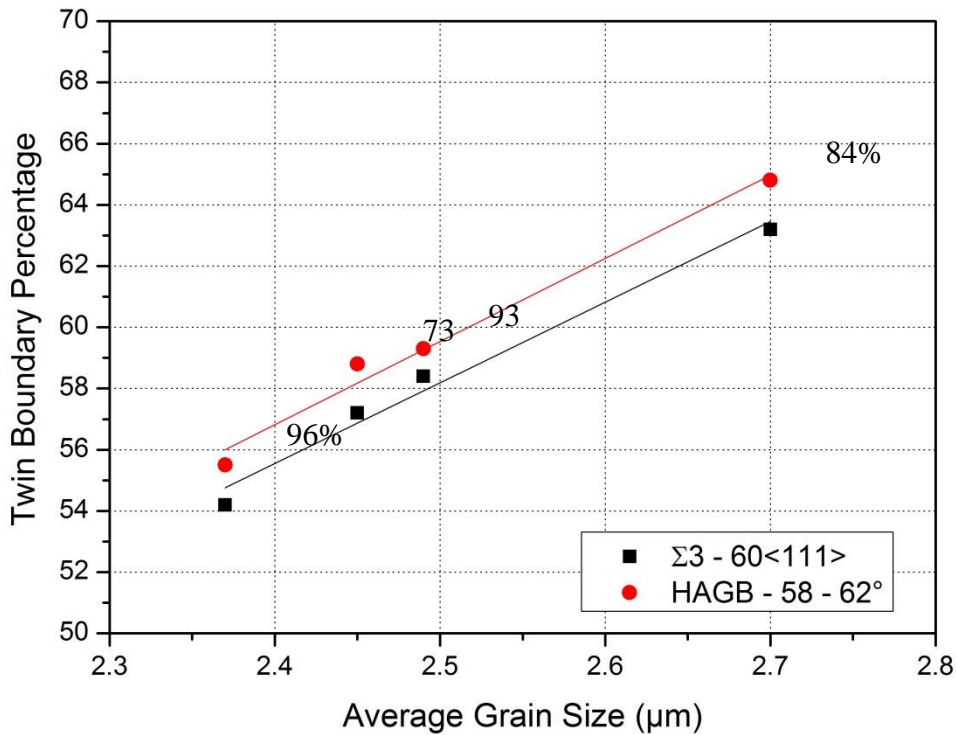


Fig. 6. Evolution of the Twin Boundary percentage as a function of the average grain size. Two different descriptions have been selected for the twin boundaries: these are described by a rotation of  $60^\circ$  around a  $\langle 111 \rangle$  axis (CSL description, tolerance angle of  $5.8^\circ$ ) (black symbols) or by a HAGB associated with an angle varying between  $58^\circ$  and  $62^\circ$  (red symbols).

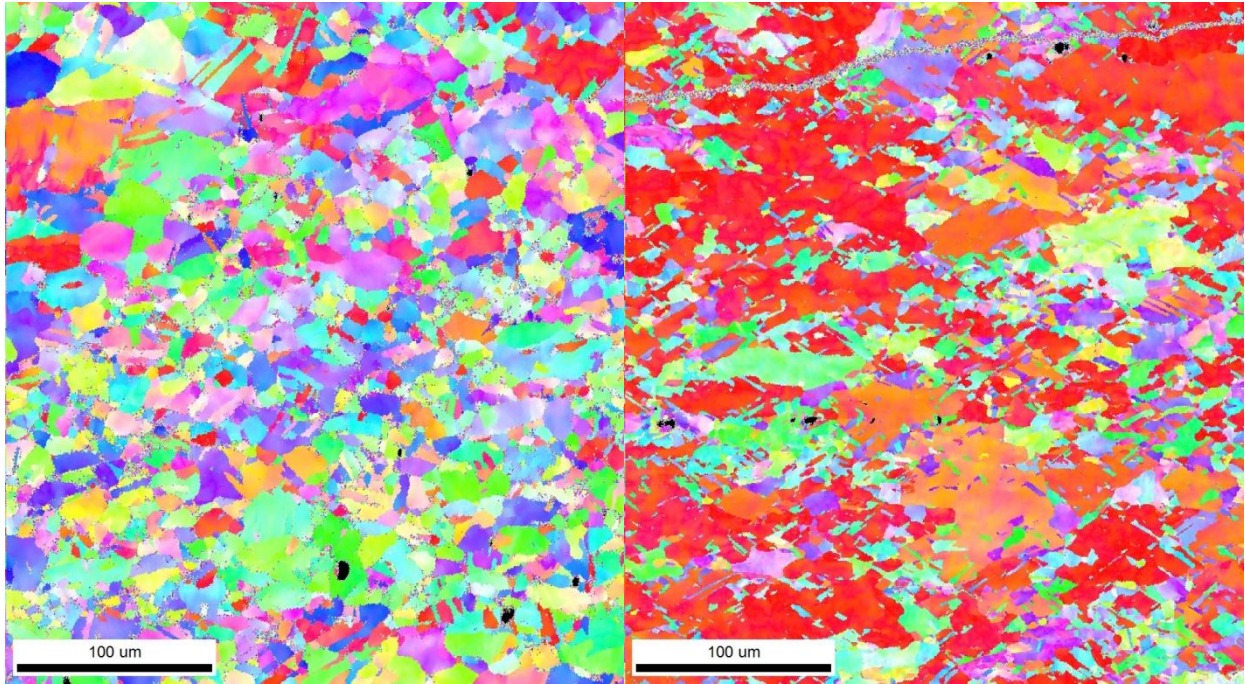


Fig. 7. EBSD orientations maps measured after 25% plastic strain for the two extreme cases: 73% CR + annealing at 350°C during 15 minutes (left) and 96% CR + annealing at 200°C during 15 minutes (right). The color code is the same as the one shown in Fig. 4 and the step size is 0.6 μm in the present case.

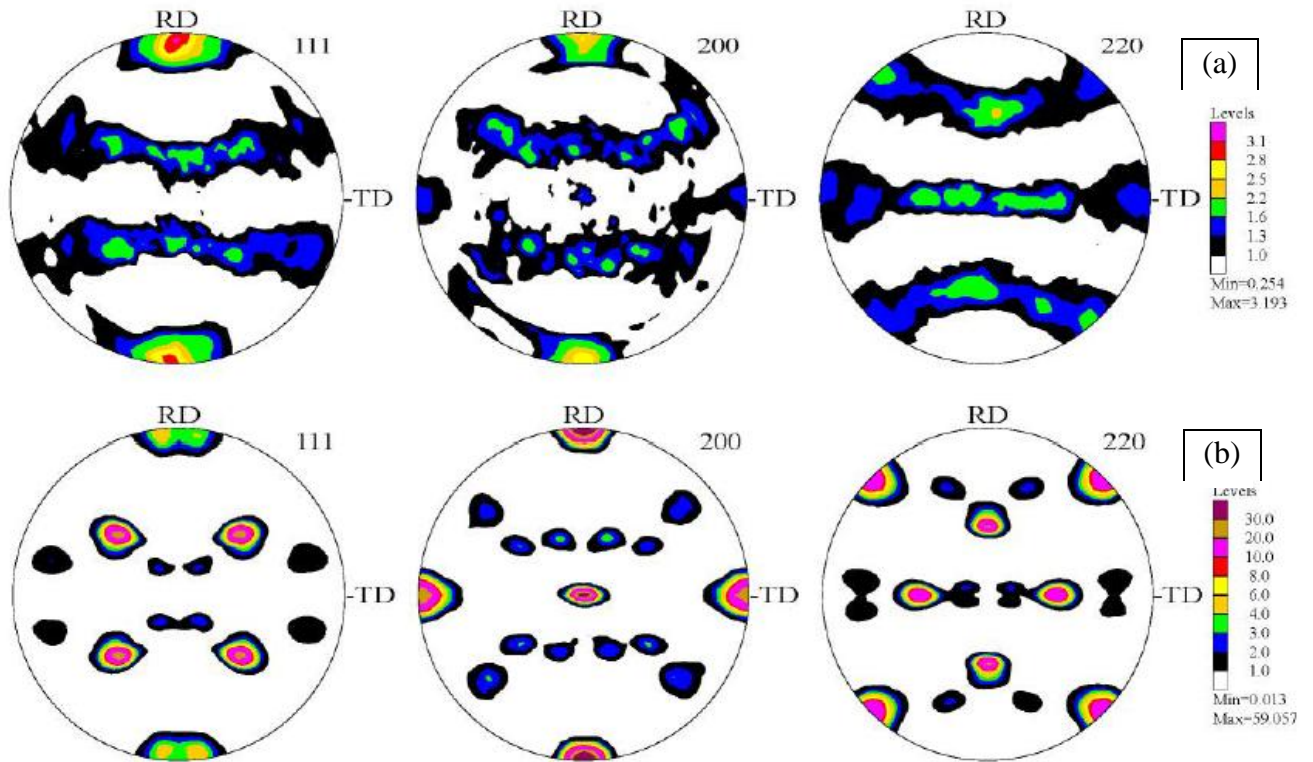


Fig. 8. Recalculated pole figures, measured by X-ray diffraction after 25% plastic strain for the two samples subjected to the two extreme thermomechanical processes : (a) 73% CR + annealing at 350°C during 15 minutes and (b) 96% CR + annealing at 200°C during 15 minutes.

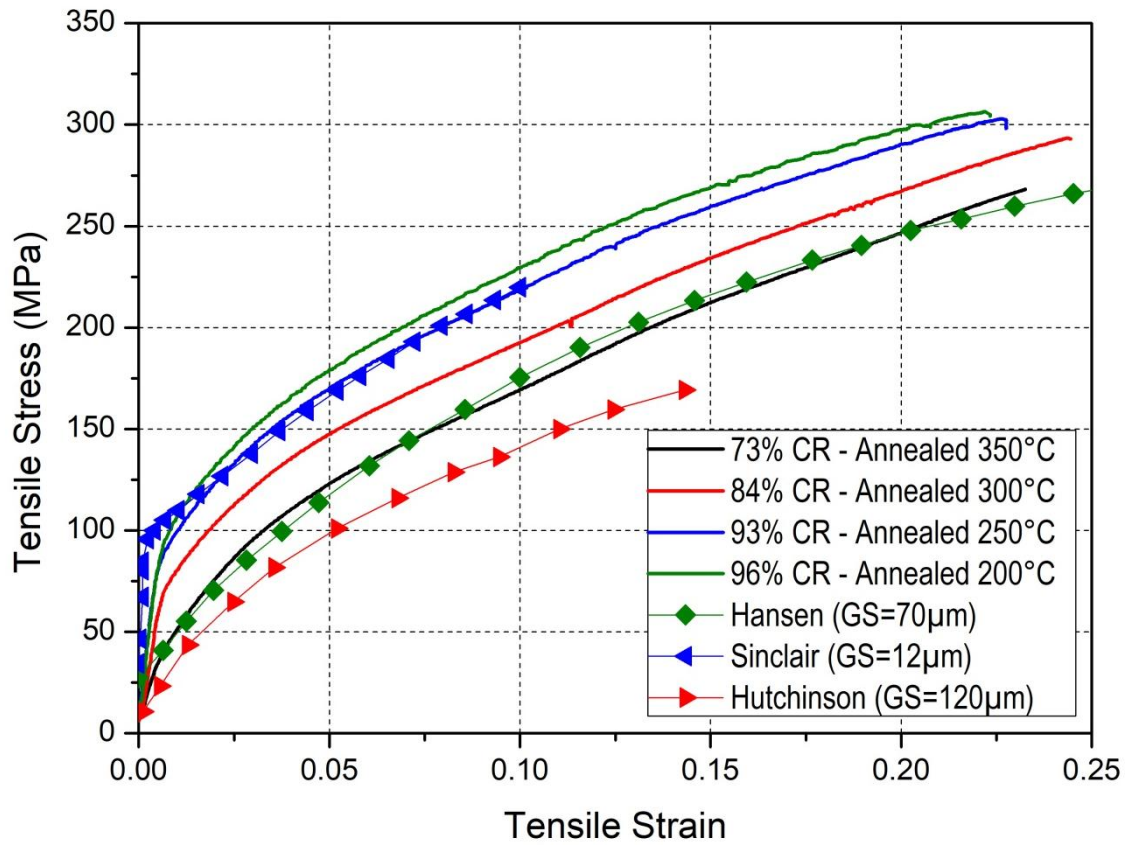


Fig. 9. Experimental tensile curves obtained after the 4 thermomechanical treatments; some other tensile curves extracted from the literature are also added for comparison. The numbers in brackets indicate the average grain size (GS) of the samples, usually determined by optical microscopy, without considering the twinned parts of the grains.

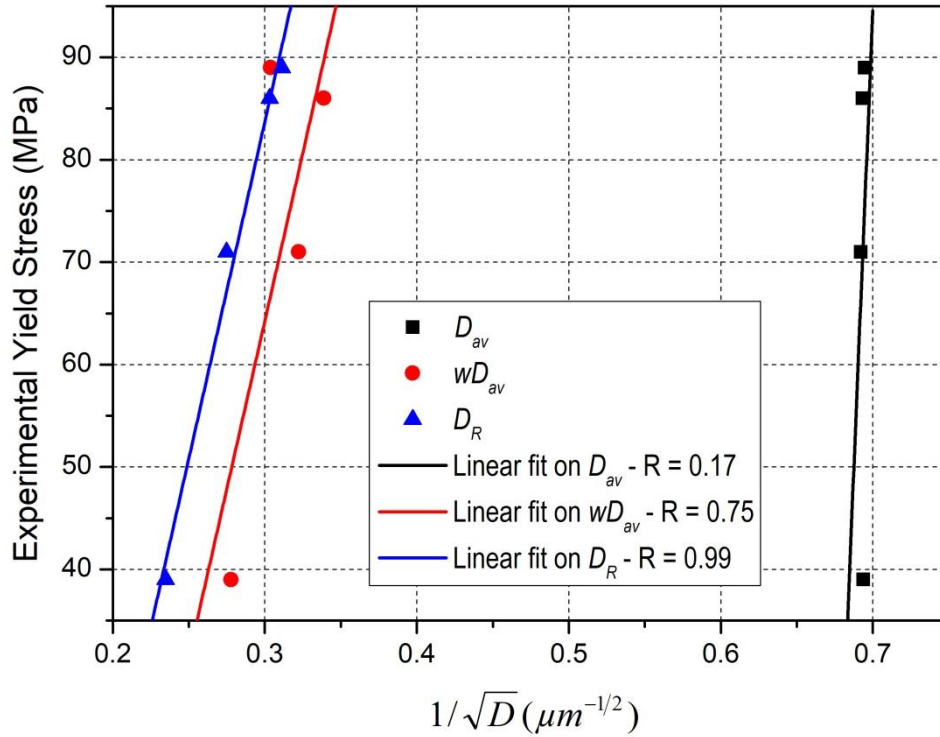


Fig. 10. Influence of the grain size on the experimental yield stress: the considered grain size is (i) the average value extracted from the EBSD maps ( $D_{av}$ ), (ii) the area weighted average grain size also extracted from the EBSD maps ( $wD_{av}$ ) or (iii) the representative grain size corrected to take into account the spread of the GS distribution ( $D_R$ ). For each linear fit performed on each set of data points, the correlation coefficient R is indicated in the legend.

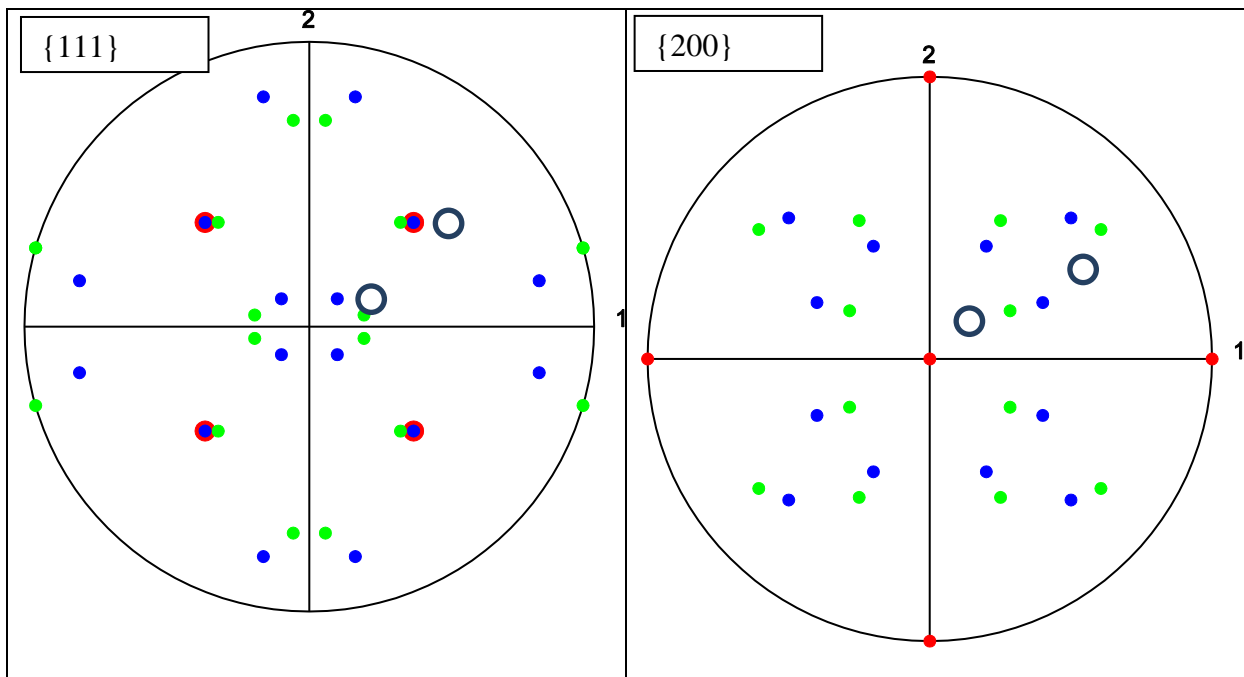


Fig. 11. Calculated pole figures indicating the positions of the  $\{111\}$  poles (left) and  $\{200\}$  poles (right) for the orientations Cube (in red), Twinned Cube (in blue) and S (in green). Open grey circles: measurement points. 1 = RD (rolling direction).

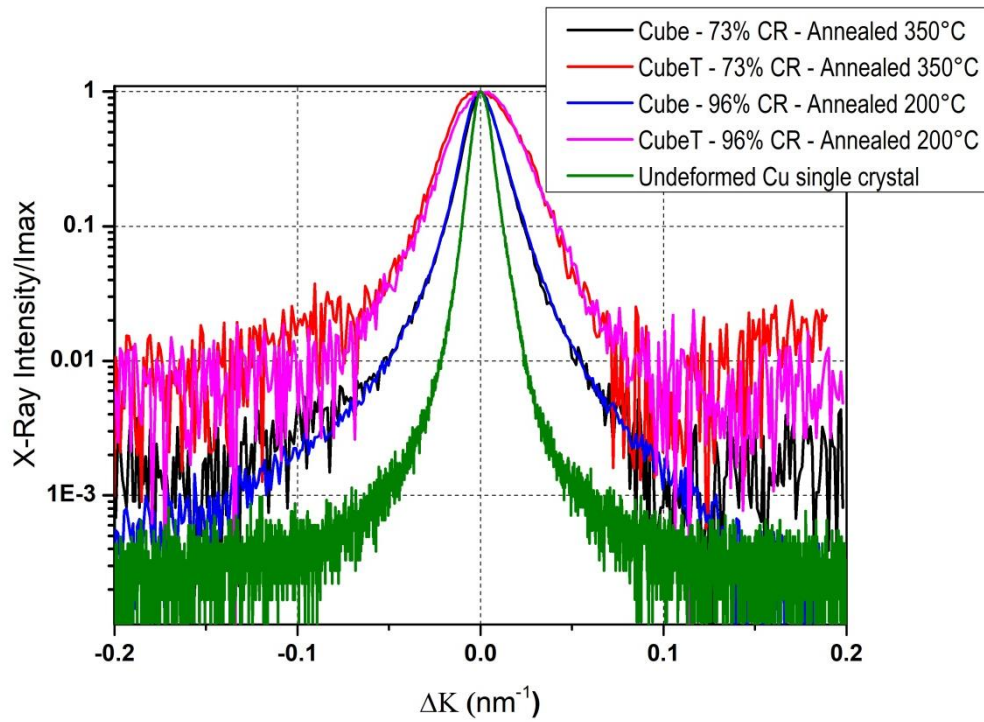


Fig. 12. {200} peaks measured in the Cube and twinned Cube (CubeT) orientations after tension for two different initial states. The measured intensities are normalized by the maximum one.  $\Delta K = 2 \left( \frac{\Delta\theta}{\lambda} \right) \cos \theta$ . A measurement performed on an undeformed single crystal has also been added as reference.

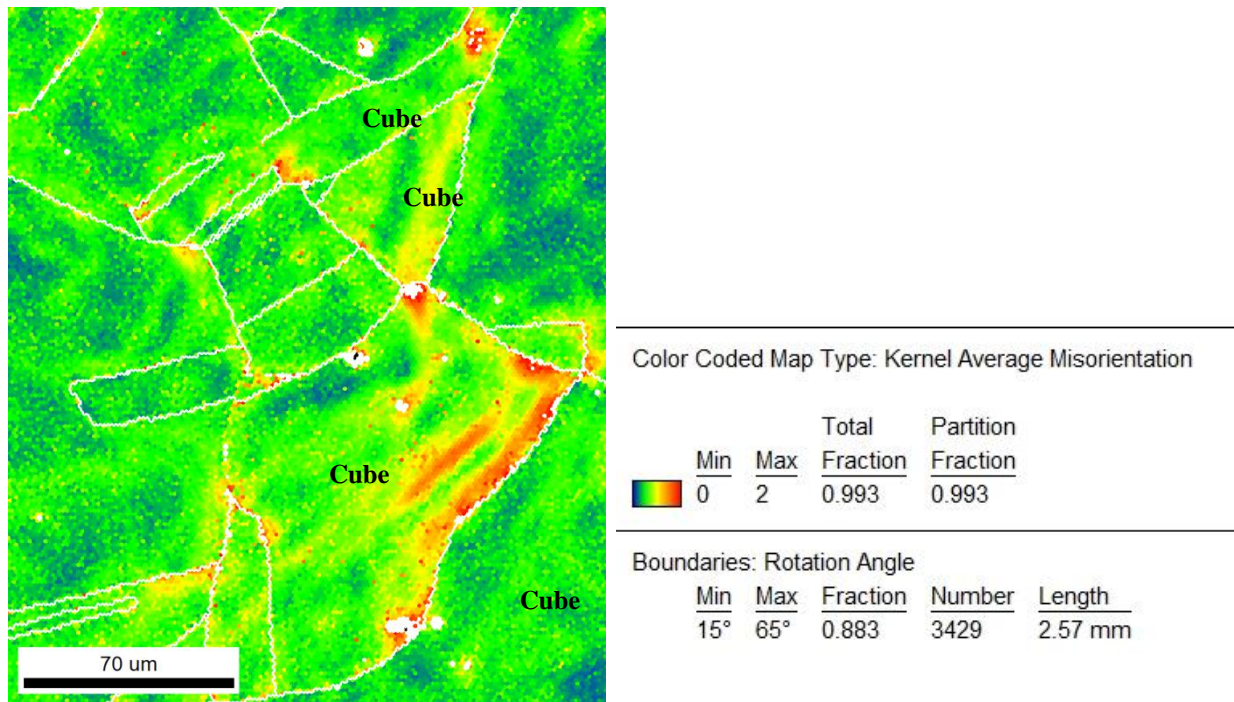


Fig. 13. EBSD map measured after 20% plastic strain for an isotropic Cu sample [45]. The color code indicates the value of the local KAM parameter between 0 and 2°.

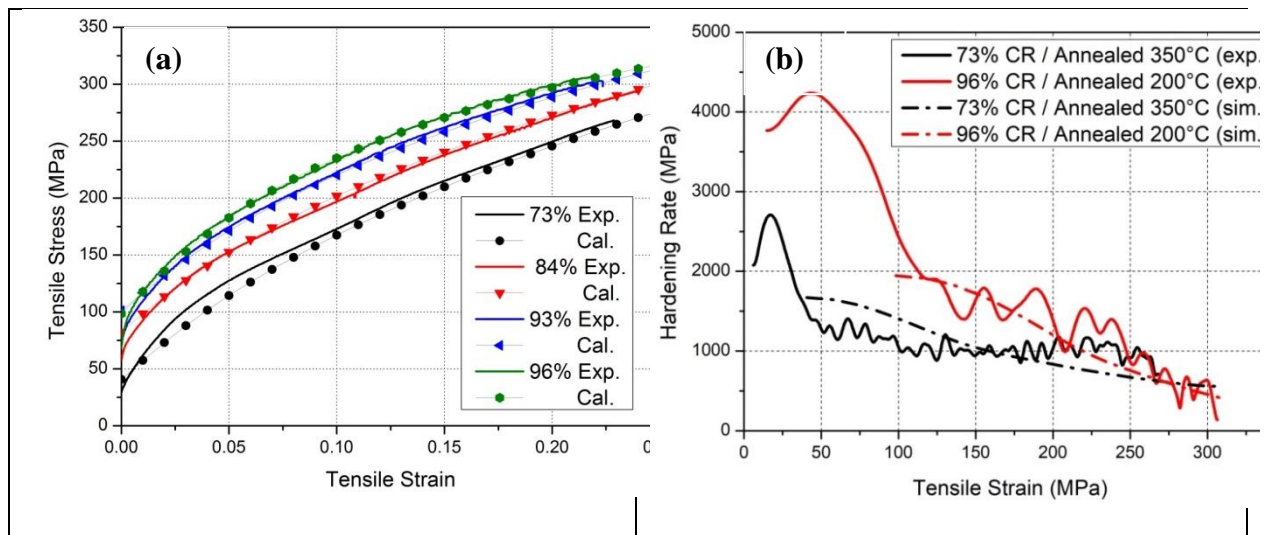


Fig. 14. Comparison of experimental and predicted plastic parts of the tensile curves (a) and hardening rates for the two extreme cases (b).

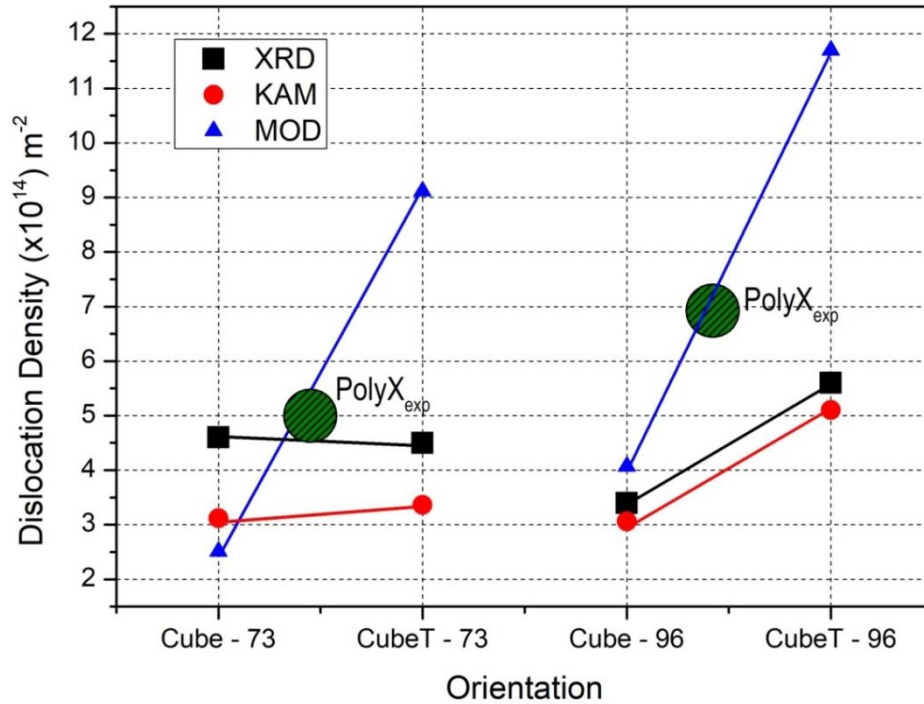


Fig. 15. Measured and calculated dislocation densities after 25% tensile strain within the two main texture components for the two materials initially rolled at 73% and 96% and annealing. The values estimated for the polycrystalline materials from the tensile curves are also indicated. The size of the symbols is proportional to the experimental error.

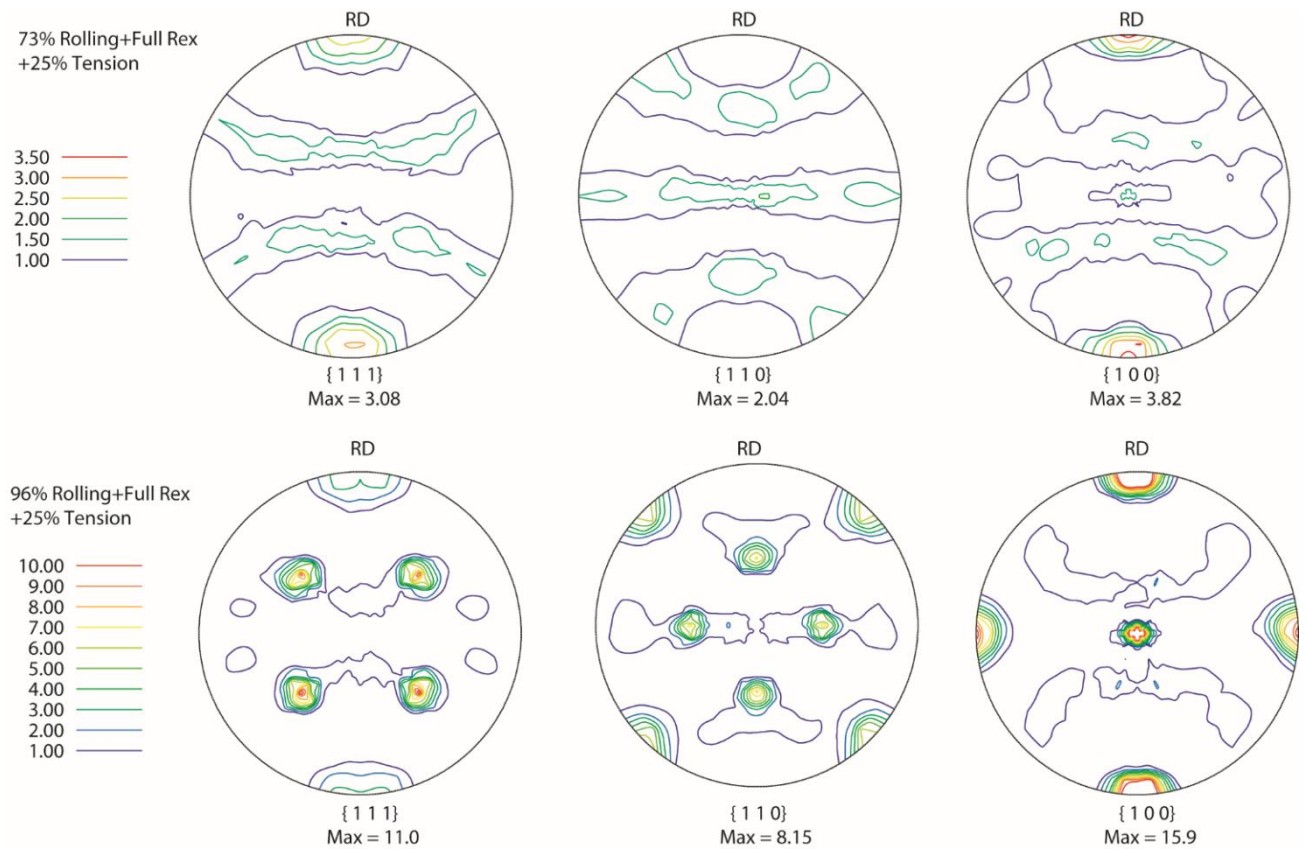


Fig.16. Predicted pole figures, for 25% plastic strain from the initial textures corresponding to the two extreme cases: 73% CR + Annealing at 350°C (15 min) and 96% CR + Annealing at 200°C (15 min).

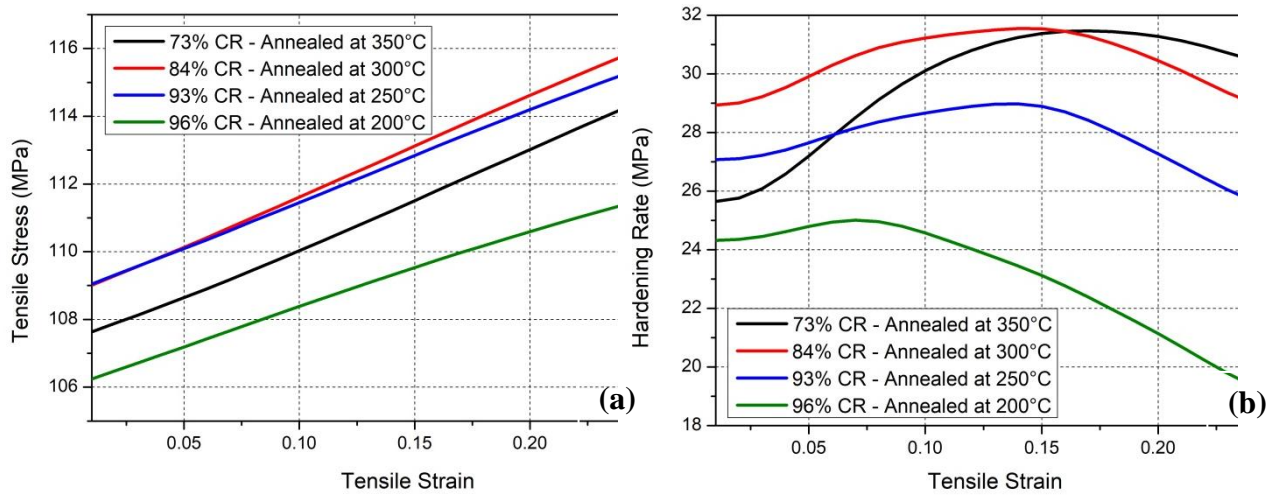


Fig. 17. Tensile (a) and hardening (b) curves, predicted by considering constant CSSs (and associated dislocation densities).

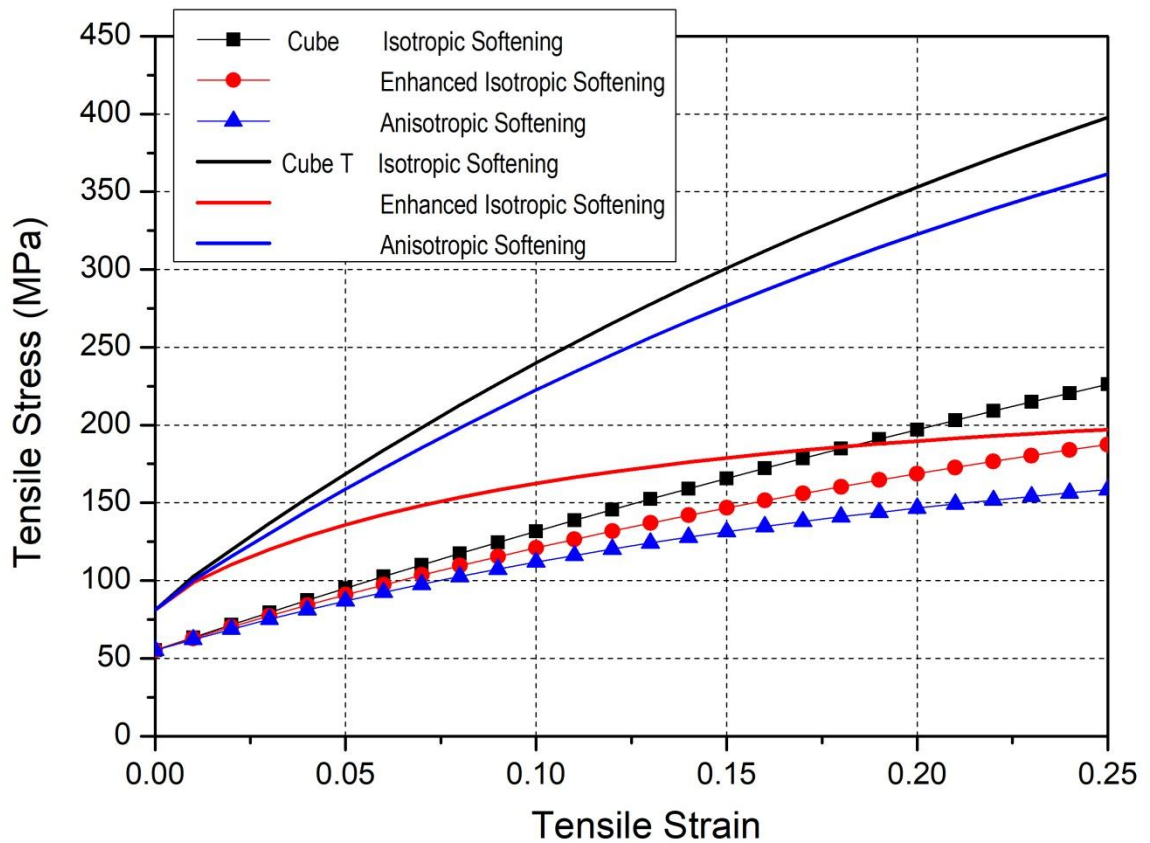


Fig. 18. Simulated tensile curves for Cube and CubeT orientations with 3 different sets of softening parameters (see Table 8).